Parameterization of Ice Crystal Conversion Processes Due to Vapor Deposition for Mesoscale Models Using Double-Moment Basis Functions. Part I: Basic Formulation and Parcel Model Results

JERRY Y. HARRINGTON, MICHAEL P. MEYERS, ROBERT L. WALKO, AND WILLIAM R. COTTON

Department of Atmospheric Science, Colorado State University, Fort Collins, Colorado

ABSTRACT

Observational data collected during the FIRE II experiment showing the existence of bimodal ice spectra along with experimental evidence of the size dependence of riming are utilized in the development of a bimodal ice spectrum parameterization for use in the RAMS model. Two ice classes are defined: pristine ice and snow, each described by a separate, complete gamma distribution function. Pristine ice is small ice consisting of particles with mean sizes less than 125 μm, while snow is the large class consisting of particles greater than 125 μm. Analytical equations are formulated for the conversion between the ice classes by vapor depositional growth (sublimation). During ice subsaturated conditions, a number concentration sink is parameterized for all ice species. The performance of the parameterizations in a simple parcel model is discussed and evaluated against an explicit Lagrangian parcel microphysical model.

1. Introduction

Increasingly, observational evidence is showing the importance of ice crystals in upper tropospheric clouds. The heat budgets, radiative properties, and microphysical characteristics of these clouds can have significant effects on the global climate feedback. Stephens et al. (1990) showed the importance of the crystal asymmetry parameter and the effective crystal size to radiative calculations and climate feedback, two variables that are not well known for cirrus clouds. Their model results showed that ice water feedback on a CO_2 warming event could be either positive or negative depending upon the choices of the above variables. Stackhouse and Stephens (1990) showed that variations in ice crystal concentrations less than about 100 μm in size can greatly affect the longwave absorption and shortwave albedo of cirrus clouds. Mitchell and Arnott (1994) have shown the importance of ice habit in radiative transfer calculations. Their results showed variations in absorption, extinction, and scattering calculations depending upon the ice habit. Even with these recent results showing the importance of cirrus clouds on global climate feedback, there has been a lack of reliable measurements upon which to base physical theories. Experimental field work, such as the First ISCCP Regional Experiment, FIRE I and FIRE II, has done much to provide recent measurements of the physical characteristics of these clouds systems.

A characteristic of cirrus clouds that may be important to numerical modelers is observational evidence showing the existence of a bimodal distribution of ice particles. Heymsfield (1975) derived ice particle spectra from measurements in cirrus uncinus clouds and showed evidence of a bimodal spectrum with a sharply peaked small-particle mode (sizes less than about 200 μm) and a broader large-particle mode (sizes greater than about 200 μm). Hein et al. (1993) showed evidence for the possible existence of large numbers of small, pristine ice crystals ($D \leqslant 50$ μm) in cirrus clouds using a forward Monte Carlo method to calculate the spectral variations of scattering and absorption of a cirrus layer. It was found that a large number of small, pristine ice crystals was required to make their spectral calculations conform to observation. This requirement may mean that the radiative properties were not represented in a physically complete fashion; however, the suggestion of a small ice class still exists. Arnott et al. (1993) presented ice replicator and 2D-C probe data showing that ice crystals in cirrus clouds can have a bimodal representation; their data showed a small-ice mode (sizes less than about 125 μm) with large number concentrations and a mode that contains larger, more massive, particles but lower number concentrations.

The above information points to the consideration of small ice as a separate category in a mesoscale cloud model such as the Regional Atmospheric Modeling System (RAMS) or in other large-scale models. Other information that also points us in this direction is the

Corresponding author address: Mr. Jerry Y. Harrington, Department of Atmospheric Science, Colorado State University, Fort Collins, CO 80523.

observational evidence of the size dependence of rim-
ing. Schlamp and Pruppacher (1977) and Pitter (1977)
showed that riming does not occur on small ice parti-
cles (ice smaller than 50–150 μm depending on the
crystalline habit); thus, these particles should only be
affected by vapor deposition and aggregation growth
processes. Our problem is, then, to develop ice classes
that conform to these observations with the ultimate
goal being implementation into a larger-scale numeri-
cal prediction model.

In past versions of RAMS (version 2c) microphys-
ical module only one class of vapor grown ice (pristine
ice) was considered (see Cotton et al. 1986). This ice
class was described mathematically by a monodisperse
distribution and was the source for all other ice cate-
gories. RAMS microphysics, as is true for many so-
called bulk microphysical packages, is designed around
the concept of using statistical distribution functions to
keep track of the concentration and mass mixing ratio
variation with size. In RAMS, we use the complete
gamma distribution function to describe the concentra-
tion and mass mixing ratio of the hydrometeor species;
this function is given by (Walko et al. 1995) as

$$n(D) = \frac{N_t}{\Gamma(\nu)} \left(\frac{D}{D_n}\right)^{\nu-1} \frac{1}{D_n} \exp\left(-\frac{D}{D_n}\right), \quad (1)$$

where ν is the distribution shape parameter (see Fig. 1
for an example of ν variation), D_n is the characteristic
diameter of the distribution,[1] N_t is the number concen-
tration of hydrometeors of a given type, and $\Gamma(\nu)$ is
the gamma function of ν and can easily be looked up
in mathematical tables. Many physical growth pro-
cesses affect the ice/liquid hydrometeor species, and
the difficulty related to this that arises in bulk micro-
physical modeling is how one keeps track of all of the
different growth processes using complete distribution
functions. If we used only a single distribution function
to mathematically describe all of the model ice, it is
easy to see that keeping track of the statistical percent-
age of mass mixing ratio and number concentration af-
fected by different growth processes would be nearly
impossible. One method, and the one that we use in
RAMS (see Walko et al. 1995), is to divide the hydro-
meteors into classes depending upon the processes that
affect them. In RAMS there are seven of these hydro-
meteor classes (cloud drops, rain, pristine ice, snow,
aggregates, graupel, and hail), and each is distributed
via the above-given gamma distribution function. In
this methodology a hydrometeor maintains its classifi-
cation (say, snow) if it is affected by a growth process
that does not change that identity. For the pristine ice
and snow categories this growth process is vapor depo-
sition; any other growth process that affects the pristine

ice or snow category causes a transfer of the appropri-
ate mass mixing ratio and concentration to a new cat-
egory.

It seems feasible, in light of the above-given data,
that the aforementioned pristine ice class used in
RAMS is not a sufficient description of vapor-grown
ice. The data seems to suggest the inclusion of a second
ice class that originates in the pristine ice class, a class
that we will call snow. The snow class will include only
vapor-grown pristine ice and lightly rimed ice but not
aggregates of pristine ice since the RAMS model al-
ready accounts for this process with a separate distri-
bution of aggregated crystals (Walko et al. 1995).
Thus, we define a class of ice (pristine ice) in which
the mean size of the ice particles is less than 125 μm
and can grow only by vapor deposition and still main-
tain its identity as pristine ice. The pristine ice crystals
can aggregate and melt. If they do, the appropriate
number concentration and mass mixing ratio are trans-
ferred to other categories. The pristine ice category is
described mathematically by its own gamma distribu-
tion function (in keeping with Walko et al. 1995). A
larger ice class (snow) is defined in view of the above
evidence in which the mean ice particle size is greater
than 125 μm and is composed of vapor-grown pristine
ice and lightly rimed ice. The snow category is also
described by its own gamma distribution function and
is allowed to rime cloud droplets, melt, and undergo
collection processes. The pristine ice and snow cate-
gories, therefore, define a bimodal spectrum of simi-
larly grown ice particles. It should be emphasized at
this point that both pristine ice and snow are mathe-
matically defined by separate complete gamma distri-
butions; thus the snow category overlaps into the sizes
smaller than 125 μm, while the pristine ice distribution
overlaps into the sizes greater than 125 μm. This arti-
ficial overlap is a consequence of using the complete
gamma distributions. It would be possible to use in-
complete gamma distributions that terminate at a given
size; however, these functions are computationally too
expensive to use in a bulk model.

During conditions of ice supersaturation and subsat-
uration a method is needed for finding the concentra-
tion and mass mixing ratio transferred between the pris-
tine ice and snow spectra. In section 2 analytical equa-
tions for this transfer process are derived. Since a
concentration sink is needed during ice subsaturated
conditions, a description of our parameterization of this
sink is described in section 3. Section 4 describes the
Lagrangian parcel model and the effects of the imposed
forcing on the ice spectra. Summary and conclusions
are given in section 5. In Part II we examine the pa-
rameterizations using two-dimensional tests with
RAMS on the 26 November 1991 FIRE II cirrus case.

2. Predictive equations

As was stated above, the ice crystals are divided into
two classes, pristine ice and snow, with the delineation

---

[1] D_n serves to nondimensionalize the distribution function and is
physically related to the mean particle size of the distribution.

between the classes defined by a boundary size (D_b). The two ice classes are described by separate, complete gamma distributions as given by Eq. (1), where $D = D(t)$ for simplicity. A plot of the model representation of these distributions for pristine ice crystals and snow is given in Fig. 1. This figure also illustrates how the choice of the parameter ν affects the shape of the distribution; here, the pristine ice distribution uses $\nu = 1$, and the snow distribution uses $\nu = 3$. The total mixing ratio, number concentration, and mean size of a given distribution are described by

$$r = \frac{1}{\rho_a} \int_0^\infty m(D)n(D)dD, \qquad (2)$$

$$N_t = \int_0^\infty n(D)dD, \qquad (3)$$

and

$$\bar{D} = \frac{\displaystyle\int_0^\infty Dn(D)dD}{\displaystyle\int_0^\infty n(D)dD} = \nu D_n, \qquad (4)$$

where r is the mixing ratio of any ice species, N_t is the number concentration, ρ_a is the density of air, $m(D)$ is the mass of any crystal with a maximum dimension of D, and $\bar{D}$ is the mean hydrometeor size of the number distribution. Note that $\bar{D}$ is related to D_n by the distribution shape parameter. The mass of a given hydrometeor is formulated in terms of a mass–dimensional relation, which is a simple function of the maximum axial length (Mitchell 1988; Mitchell and Arnott 1994),

$$m = \alpha_m D^{\beta_m}, \qquad (5)$$

where α_m and β_m are numerical constants that vary with crystal habit. Values of these constants can be found in the mentioned references.

In developing the predictive equations for the bimodal ice spectrum, let us first consider the effects of vapor depositional growth on the mixing ratio of any given ice distribution. If we differentiate (2) with respect to time, we find

$$\dot{r} = \frac{1}{\rho_a} \int_0^\infty \left(\frac{\partial m(D)}{\partial t} n(D) + m(D) \frac{\partial n(D)}{\partial t} \right) dD. \qquad (6)$$

By using the appropriate relations (see appendix A for details), we can derive the following:

$$\dot{r} = \frac{1}{\rho_a} \int_0^\infty \frac{dm}{dt} n(D)dD. \qquad (7)$$

The rate dm/dt is an equation for the mass growth of the ice particles; here we are considering vapor growth only, so dm/dt takes the form (Byers 1965)
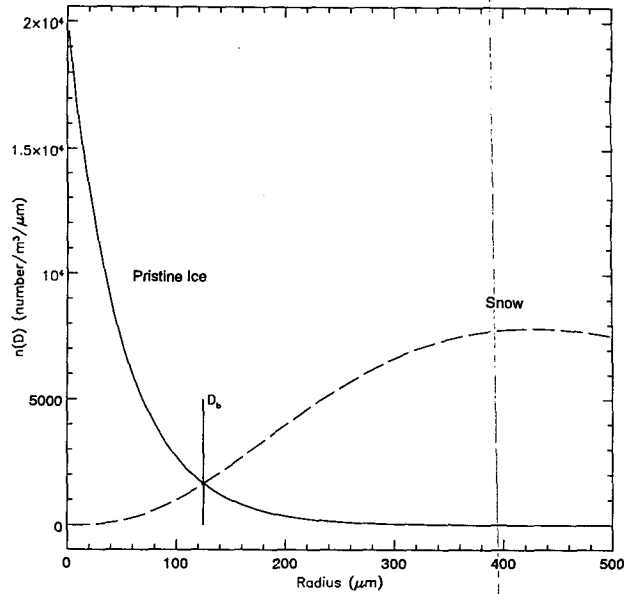

FIG. 1. Model representation of the bimodal ice distributions of pristine ice (solid) and snow (dashed). The pristine ice distribution has a shape factor of $\nu = 1$, while snow is $\nu = 3$. The delineation between the ice categories is defined by the cut diameter D_b.

$$\frac{dm}{dt} = 4\pi C_i(S_i - 1)G_i(T, P)\bar{f}_{\nu,L*}, \qquad (8)$$

where C_i is the crystal capacitance term, S_i is the ice saturation, $\bar{f}_{\nu,L*}$ is the ventilation coefficient, and $G_i(T, P)$ is a function of temperature and pressure. The function $G_i(T, P)$ is defined as (Pruppacher and Klett 1978)

$$G_i(T, P) = \left[\frac{R_\nu T}{e_{s,i} D_\nu} + \frac{L_s}{k_a T}\left(\frac{L_s}{R_\nu T} - 1 \right) \right]^{-1}, \qquad (9)$$

where R_ν is the gas constant for water vapor, T is the environmental temperature, $e_{s,i}$ is the saturation vapor pressure over ice, D_ν is the diffusivity of water vapor, L_s is the latent heat of sublimation, and k_a is the thermal diffusivity of air. The ventilation coefficient used here is for oblate spheroids and is given in Pruppacher and Klett (1978) as

$$\bar{f}_{\nu,L*} = 1 + 0.14X^2 \quad \text{for} \quad X = N_{Sc,\nu}^{1/3}N_{Re,L*}^{1/2} < 1$$

$$= 0.86 + 0.28X \quad \text{for} \quad X \geq 1, \qquad (10)$$

where $N_{Re,L*}$ is the Reynolds number with the significant dimension, $L*$ being the ratio of the surface area to the perimeter of the crystal, and $N_{Sc,\nu}$ is the Schmidt number. The surface area and perimeter of plates and hexagonal plates is easy to calculate. For a needle crystal we use the perimeter formulation given in Pruppacher and Klett (1978) for a prolate spheroid of the same aspect ratio of the needle crystal. The surface area of a needle is approximated as the surface area of the

prolate spheroid; this value is easy to calculate by using the area of a surface of revolution.

Recently, more accurate forms of the vapor depositional growth relation have been formulated (Srivastava and Coen 1992) because the linear temperature profile between the crystal and the environment assumed by (8) above causes significant errors, especially when sublimation regimes are encountered. Instead of using the quadratic approximation to saturation vapor density at the particle surface as derived by Srivastava and Coen (1992), we use the method of Walko et al. (1995), which uses a bounded value to the reference temperature in the expansion of the Clausius–Clapeyron equation (see Walko et al. 1995 for details).

The capacitance term in (8) is a function of a maximum and minimum dimension, c and a, respectively. Simplification of the capacitance term is needed in order to arrive at an analytical solution to (7). This may be done by writing C_i as a function of the aspect ratio $A = c/a$ and its maximum dimension $c = D$. Therefore,

$$C_i = C_i(c, a) = g(A, D) = \chi(A)D, \quad (11)$$

where $\chi(A)$ is a function of the aspect ratio. The function $\chi(A)$ is a constant function of a given aspect ratio, which now allows the dm/dt equation to be integrated over the distribution functions. Note that $\chi(A)$ is also a function of the crystalline habit. The aspect ratio of any given ice crystal is not held constant throughout the simulation, however. Bulk values of the aspect ratio for the entire distribution of ice is determined by equating (5) to an equivalent volume (see appendix B for details of $\chi(A)$ and the bulk aspect ratio method).

Substituting Eqs. (8) and (11) in (7) gives

$$\dot{r} = \int_0^\infty \Psi D n(D) dD, \quad (12)$$

where

$$\Psi = 4\pi\chi(A)(S_i - 1)G_i(T, P)\overline{f}_{\nu,L*}. \quad (13)$$

Using the definition of the complete gamma function from Abramowitz and Stegun (1972)

$$\Gamma(n) = \int_0^\infty X^{n-1} \exp(-X) dX \quad (14)$$

and the moments of the gamma distribution given by

$$I(P) = \int_0^\infty D^P n(D) dD = \frac{N_t}{\Gamma(\nu)} D_n^P \Gamma(\nu + P), \quad (15)$$

where P refers to the Pth moment of the distribution function, then (12) can be written in a very simple final form as

$$\dot{r} = \frac{\Psi}{\rho_a} \frac{N_t}{\Gamma(\nu)} D_n \Gamma(\nu + 1) = \frac{\Psi}{\rho_a} I(1). \quad (16)$$

Equation (16) is the expression used for the vapor depositional growth of a given distribution of ice crystals.

Calculations of the transfer of crystals between the pristine ice and snow distributions can be accomplished by considering the shift in the ice spectra due to the growth or sublimation of the distribution given by Eq. (16). Consider Fig. 2, where a given distribution of pristine ice has evolved during a model time step Δt. In this time the distribution has broadened and some pristine ice mass and number concentration has been transferred across the boundary given by D_b. By calculation of the number concentration and mass mixing ratio fluxes across this boundary, it is possible to describe the crystal number concentration and mixing ratio that should be transferred between the distributions. This transfer is dependent upon the ice supersaturation, which will determine the direction of the number concentration and mixing ratio fluxes. In an ice supersaturated regime the transfer of number concentration and mixing ratio from the pristine ice to the snow distribution can be described by the following relation:

$$\dot{r}_p^f = \frac{d}{dt} \frac{1}{\rho_a} \int_{D_b}^\infty m(D) n_p(D) dD \quad (17)$$

and

$$\dot{N}_p^f = \frac{d}{dt} \int_{D_b}^\infty n_p(D) dD, \quad (18)$$

where the above describe the change in the number concentration and mass mixing ratio in the region $D_b \to \infty$ (the region defined as snow). For example, during ice supersaturated conditions, the number change in this region must be due to crystals that were once
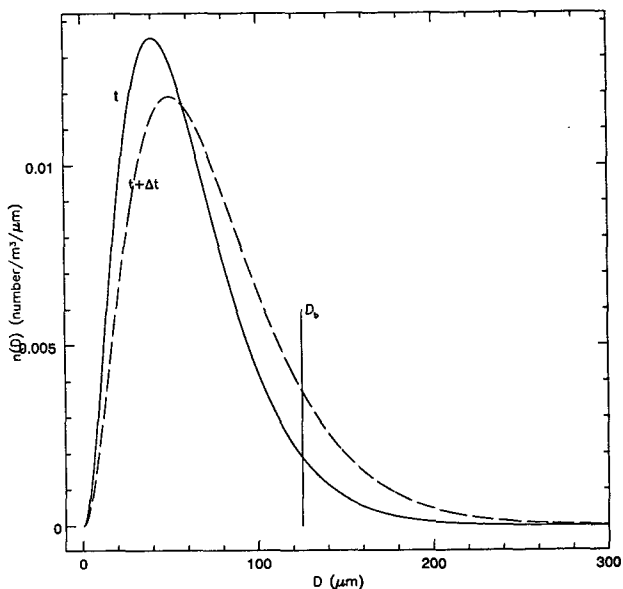

FIG. 2. The time change in the complete gamma distribution for $\nu = 3$. The distribution at $t + \Delta t$ has undergone ice crystal growth by vapor deposition.

smaller than D_b since no other source into this region exists. The subscript p in the above equations is for transfer from pristine ice to snow. By using Leibnitz' rule, Eq. (42), and the chain rule, it is possible to arrive at the following forms of the transfer equations; see appendix C,

$$\dot{N}_p^f = \left.\frac{dD}{dt}\right|_{D=D_b} n_p(D_b) \qquad (19)$$

and

$$\dot{r}_p^f = \frac{1}{\rho_a} m(D_b) \left.\frac{dD}{dt}\right|_{D=D_b} n_p(D_b)$$

$$+ \frac{1}{\rho_a} \int_{D_b}^{\infty} \frac{dm}{dt} n_p(D)dD. \qquad (20)$$

Equation (19) is interpreted as the number concentration of pristine ice that grows by vapor deposition beyond the threshold size D_b (this is graphically illustrated in Fig. 3a). This defines the flux of pristine ice to snow. Equation (20) has two terms that describe the total change in the region $D_b \rightarrow \infty$. The first term in (20) describes the amount of pristine ice mixing ratio associated with smaller pristine ice crystals that grow larger than D_b and, thus, enter the region $D_b \rightarrow \infty$. The second term in (20) describes the vapor depositional growth of pristine ice crystals larger than D_b (since this is a complete distribution). Figure 3b illustrates this process. In principle the transfer equations should not include the second term because it does not describe a mass transfer from the region $0 \rightarrow D_b$ to $D_b \rightarrow \infty$ but describes the vapor depositional growth of mass in $D_b \rightarrow \infty$. This term exists only because we are dealing with complete distributions. We choose to include this growth term in the transfer equation because it is im-
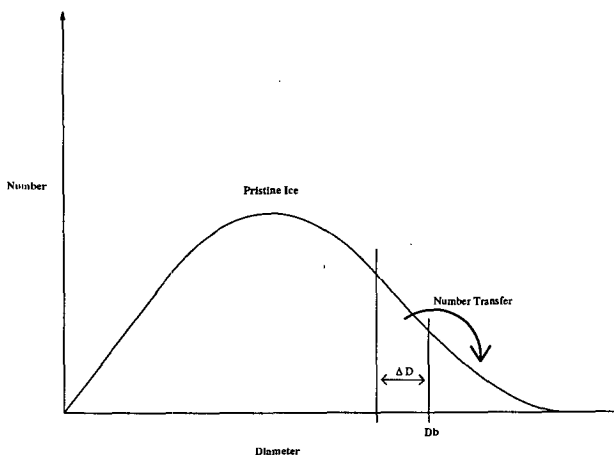

FIG. 3a. Illustration of the concentration transfer from pristine ice to snow. Equation (19) describes the concentration in a region of the distribution (that is dependent upon dD/dt) that will be transferred beyond the bounding size D_b.
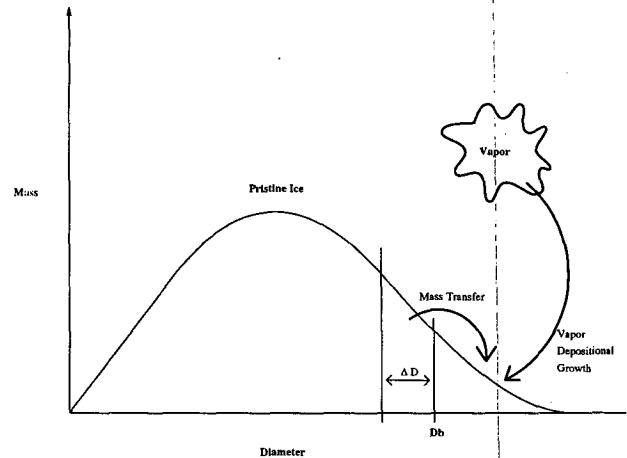

FIG. 3b. Illustration of the mass mixing ratio transfer from pristine ice to snow. This illustrates the two parts of Eq. (20) that affect the sizes larger than D_b. The first term on the right-hand side of Eq. (20) describes the mass transferred, while the second term describes the growth of the particles larger than D_b.

portant to keep the percentage of mass in the distribution tail to a minimum. Since we are dealing with complete distributions, it is impossible to reduce to zero any mass or number concentrations that overlap. Keeping this growth term avoids excessive accumulation in the pristine ice distribution and tends to keep the mean diameters of both pristine ice and snow within realistic bounds.

In order to solve (19) and (20) we invoke the definition of the incomplete gamma function from Abramowitz and Stegun (1972)

$$\Gamma(n, Y) = \int_Y^{\infty} X^{n-1} \exp(-X)dX \qquad (21)$$

and define the moments of the incomplete gamma distribution as

$$T_I(P, Y) = \int_Y^{\infty} D^P n_I(D)dD$$

$$= \frac{N_{t,I}}{\Gamma(\nu)} D_{n,I}^P \Gamma\left(\nu_I + P, \frac{Y}{D_{n,I}}\right), \qquad (22)$$

where $T_I(P, Y)$ is the Pth moment of the incomplete gamma distribution I. Combining (6) and (8), we get an expression for dD/dt as

$$\frac{dD}{dt} = \Phi D^{2-\beta_m}, \qquad (23)$$

where

$$\Phi = \frac{4\pi\chi}{\alpha_m \beta_m} (S_i - 1)G_i(T, P)\bar{f}_{\nu,L*}. \qquad (24)$$

By using these expressions in Eqs. (19) and (20), the final forms become

$$\dot{r}_p^f = \frac{\Phi}{\rho_a} \alpha_m D_b^2 n_p(D_b) + \frac{\Psi}{\rho_a} T_p(\nu + 1, D_b/D_n) \quad (25)$$

and

$$\dot{N}_p^f = \Phi D^{2-\beta_m} n_p(D_b). \quad (26)$$

These equations are the prognostic equations for the transfer of pristine ice mixing ratio and number concentration to snow during ice supersaturated conditions. Use of these equations requires the calculation of the incomplete gamma functions every time step, which is computationally inefficient in a bulk model. We, therefore, choose to make lookup tables of these functions for code efficiency. Since ν and D_b are constant throughout any simulation, we need only construct a one-dimensional table of the form

$$T(D_n) = \Gamma\left(\nu + 1, \frac{D_b}{D_n}\right). \quad (27)$$

Our table only needs to contain realistic increments of and range over realistic values of D_n.

In the case of ambient conditions that are subsaturated with respect to ice, the transfer of snow number concentration and mass mixing ratio to the pristine ice crystal class can be described by considering the shift of the snow distribution in the region $0 \rightarrow D_b$. This process is graphically similar to the processes portrayed in Figs. 3a and 3b except that the region $0 \rightarrow D_b$ of the snow distribution is considered. The change in the snow distribution in the region $0 \rightarrow D_b$ can be written

$$\dot{r}_s^f = \frac{d}{dt} \frac{1}{\rho_a} \int_0^{D_b} m(D) n_s(D) dD \quad (28)$$

and

$$\dot{N}_s^f(D) = \frac{d}{dt} \int_0^{D_b} n_s(D) dD. \quad (29)$$

Using Leibnitz' rule, (42), and the chain rule, it is possible to cast the snow transfer equations into the following forms:

$$\dot{N}_s^f = - \left. \frac{dD}{dt} \right|_{D=D_b} n_s(D_b) \quad (30)$$

and

$$\dot{r}_s^f = -\frac{1}{\rho_a} m(D_b) \left. \frac{dD}{dt} \right|_{D=D_b} n_s(D_b)$$
$$+ \frac{1}{\rho_a} \int_0^{D_b} \frac{dm}{dt} n_s(D) dD. \quad (31)$$

Equation (30) is a simple function of the rate of change in particle size evaluated at the boundary. This gives the change in concentration that occurs in the region $0 \rightarrow D_b$, which must be due to snow transfer since there is no other process that affects N_s built into these equa-

tions. Equation (31), as (25) above, has two distinct physical parts: The first term in (31) describes the change in the snow distribution in the region $0 \rightarrow D_b$ due to the transfer of mass mixing ratio from the region $D_b \rightarrow \infty$. The second term on the right-hand side of (31) describes the loss of snow mass mixing ratio in the region $0 \rightarrow D_b$ due to sublimation. This term represents loss of snow mass mixing ratio to the vapor state, which is accounted for in Eq. (16); hence, we choose to drop this term since we are interested in the transfer of snow to pristine ice.

This may seem mathematically inconsistent with our choice to keep the term describing the vapor depositional growth of pristine ice larger than D_b in size. This choice is, however, physically consistent since in the ice supersaturated case the mass growth of the pristine ice that is greater than D_b in size is a source of ice mass and is actually in the region defined as snow. The case of ice subsaturation is distinctly different since the second term in (31) describes snow sublimation that is a source of vapor.

The solution to Eqs. (30) and (31) above, using (23), becomes

$$\dot{r}_s^f = - \frac{\Phi}{\rho_a} \alpha_m D_b^2 n_s(D_b) \quad (32)$$

and

$$\dot{N}_s^f = - \Phi D_b^{2-\beta_m} n_s(D_b). \quad (33)$$

Equations (32) and (33) describe the flux of number concentration and mass mixing ratio from the snow to the pristine ice class in conditions that are subsaturated with respect to ice. Equations (16), (25), (26), (32), and (33) make up the full set of transfer equations for the two moment predictions of the bimodal ice distributions.

Under ice subsaturated conditions, however, some of the mass that is lost to vapor comes from crystals that sublimate completely to vapor. This constitutes a number concentration sink and is discussed in the next section.

3. Sublimational number concentration loss of ice to vapor

A parameterization of the process of sublimational concentration loss from the ice distributions is considered in this section. Conditions that are ice subsaturated cause a buildup of pristine ice number concentrations unless a sink is defined. Physically, the smallest ice crystals in the distribution will disassociate to vapor in some time step Δt. It is possible to describe number concentration loss by finding the largest size crystal, D_{max}, that will sublimate completely to vapor in a given time step Δt by using the vapor depositional growth equation and then integrate the number distribution function to this size. This procedure would, again, be computationally expensive since it would require calculation of the incomplete gamma function at every

time step. Tabulation of the above functions would also not be very feasible because a two-dimensional table of dimensions (D_{max}, D_n) would have to be created. Since both D_{max} and D_n vary widely, the table would have to be quite large. This method might have been feasible if our cloud model had only one ice species; however, RAMS has seven different hydrometeor species to consider, and a two-dimensional table for each species would increase computational costs.

Our approach centers around the hypothesis that the fractional number concentration loss

$$\frac{\text{number lost to sublimation}}{\text{total concentration}} = \frac{\dot{n}\Delta t}{n_{tot}} \quad (34)$$

is a strong function of the fractional mass loss ($\dot{r}\Delta t/r_{tot}$). Here, we are hypothesizing that a certain mass loss to vapor from the distribution will give rise to a certain concentration of small ice that will sublimate in a time step. To test this hypothesis we have set up a bin representation of the various distributions and allow them to slowly sublimate over time.

Consider the established distribution shown in Fig. 4 with $\nu = 3$. To initialize the bin representation, the range of the distribution $(0 \to D_{max})$ is divided into a certain number of bins (N_{bins}) by defining each bin in terms of a specific diameter range, ΔD, where $\Delta D = N_{bins}/D_{max}$ and i denotes the ith bin. To complete the bin representation of the distribution, the number and mass in each bin needs to be specified. This is accomplished by the use of the following relations:

$$N_i = n(D_i)\Delta D$$

$$= \frac{1}{\Gamma(\nu)}\left(\frac{D_i}{D_n}\right)^{\nu-1}\frac{1}{D_n}\exp\left(-\frac{D_i}{D_n}\right)\Delta D \quad (35)$$

and

$$M(D_i) = \frac{1}{\rho_a}m(D_i)N_i, \quad (36)$$

where $n(D_i)$ is the normalized gamma distribution, $m(D_i)$ is defined by using (3), and D_i is the mean size in the given bin. The total mass in the distribution is also needed in order to define the mass loss ratio and is defined by

$$r_{tot} = \sum_{i=0}^{N_{bins}} M(D_i). \quad (37)$$

Note that, since (35) is normalized, $n_{tot} = 1$.

Using this representation, the model is run using time steps (chosen by the model) that are small enough to resolve a user-defined increment of X% in the $\dot{r}\Delta t/r_{tot}$ and $\dot{n}\Delta t/n_{tot}$ ratios. During these runs values of S_i, D_n, T, P, ν, and the crystal habit are held constant. The total time for the run is found by integrating (23) to find the time needed to completely sublimate the largest crystal (D_{max}) in the distribution.

Tabulation of the relationship between the $\dot{r}\Delta t/r_{tot}$ and $\dot{n}\Delta t/n_{tot}$ ratios is accomplished by using the growth
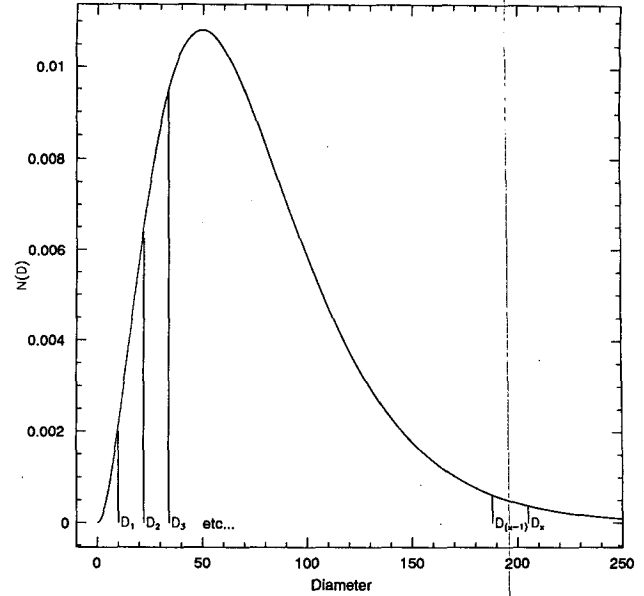

FIG. 4. Bin representation: An example of the bin representation of the gamma distribution. The distribution is divided into x number of bins of a given diameter defined by $D_i = D_{i-1} + \Delta D$.

equations (8) and (23). Mass is lost to vapor during each time step using Eq. (8). This loss in mass causes the sizes of the crystals in each bin to decrease. Number concentration losses occur by considering the largest size crystal (or the largest mass) that will completely dissociate into vapor during a given time step Δt. Since this size will rarely be the same as any bin boundary size, we must consider the concentration lost from the fraction of a bin. This is easily accomplished by considering the maximum size that dissociates and the equation for the distribution, $n(D)$. From these two quantities we can get a ΔD_{frac} by considering the bin within which the calculated maximum size exists and, then, using the lower bound to calculate ΔD_{frac}. For example, if the maximum size that will dissociate in a time step is given by D_{diss} and it lies between two bounding bin sizes, D_i and D_{i+1}, then we can calculate $\Delta D_{frac} = D_{diss} - D_i$. The fraction of number concentration from the bin can then be calculated by finding $n(\bar{D})\Delta D_{frac}$, where $\bar{D}$ is the mean size in $D_i \to D_{diss}$. By summing the concentration of crystals that disassociate to vapor in each bin and forming the ratio of this to the total concentration, we can develop a one-dimensional table of the concentration loss as it depends on $\dot{r}\Delta t/r_{tot}$.

The sensitivity of the physical parameters S_i, T, P, D_n, ν, and crystal habit to the mass and number loss ratios were tested in simulations in which these physical parameters were varied over a wide range of values. Figure 5a shows the generated curves of mass loss ratios plotted against number concentration loss ratios. In these simulations temperature, pressure, and mean
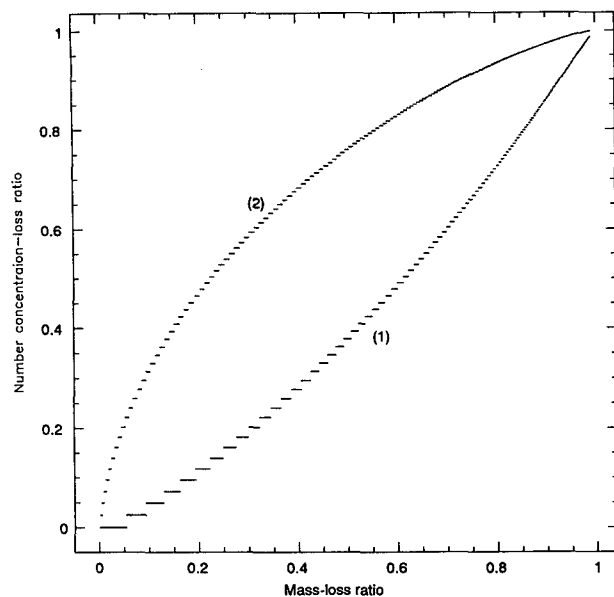
FIG. 5a. Plots of $(\dot{r}\Delta t)/r_{tot}$ vs $(\dot{n}\Delta t)/n_{tot}$: Curve 1 is for needles, and curve 2 is for hexagonal plates. Variation is over the range $S_i = 0.1 \rightarrow 0.9$.
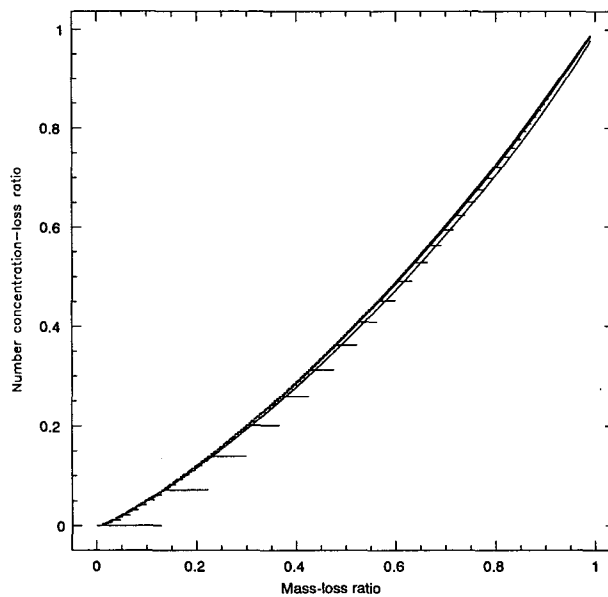
FIG. 5b. Plots of $(\dot{r}\Delta t)/r_{tot}$ vs $(\dot{n}\Delta t)/n_{tot}$: This simulation was conducted for needle crystals only. Model variations in external parameters are over the ranges of pressure $P = 600 \rightarrow 200$ mb, temperature $T = -30 \rightarrow 30°C$, and distribution mean diameter $\bar{D} = 10 \rightarrow 300$ μm.

diameter were all held fixed; also the runs were done for needles and for hexagonal plates. The variation in S_i for needles is most important for small mass loss ratios where variation can be as large as 50%–75% with respect to a given value of S_i. We choose to accept this since such a low loss of concentration will not affect results too largely. The most important variations are where $\dot{r}\Delta t/r_{tot}$ gets larger, and at these points the parameterization works well. Note that this S_i variation does not have as large an impact in the case of hexagonal plates.

Figure 5b shows a plot of the mass loss and number concentration loss curve with variation over ranges in P, T, and $\bar{D}$; S_i was set to 0.8 and the distribution shape was assumed to be Marshall–Palmer ($\nu = 1$). Simulations were done over these different ranges in order to test as many cases as possible that may cause deviations in the curve. Note, however, that there is little variation in the curve for the sublimational loss ratios over the given ranges. The widest variations shown are due to the diameter variation; the error bars indicate the maximum variation due to changes in D_n. Still, it is possible to parameterize the number concentration loss lookup tables with values of these parameters set at values that define the bulk average of the curve. Errors associated with the removal of $\bar{D}$ from the tables are around a maximum of about 38%. Similar results can be shown for different values of the ν and for different habits; however, these are not produced here.

The parameters that do cause significant shifts in the loss curves are ν and the crystal habit. Here, P, T, $\bar{D}$,

and S_i were held fixed so that the variation due to habit and ν is pronounced. Figure 6a shows plots of the mass loss and number concentration loss ratios for different values of ν. As ν increases, the mass loss ratio needed for significant concentration loss increases. This is because as ν increases, the concentration is weighted more to the larger sizes and, therefore, to larger masses.

Figure 6b shows the sensitivity of the mass loss ratio versus number concentration loss ratio to the choice of habit. Again, note the shift in the curve due to this choice. Of particular interest is that for spheres the percentage number concentration loss is larger initially for any given percentage mass loss, with this tendency reversing as the ratios approach 1. The opposite trend is observed for needles, with large initial percentage mass losses being needed in order to see any appreciable change in the percentage number concentration loss. The reason for this shift in the curve due to the different habits is related to the mass–diameter relationship, given by Eq. (5), for spheres, $\beta_m = 3$, while for needles $\beta_m \approx 1.8$ (Mitchell 1988). This power influences the way in which the given crystals evaporate. The equation for dD/dt, (23), is a function of $D^{2-\beta_m}$ and is the reason for the observed shifts in the curves. For spheres, $2 - \beta_m = -1$ giving a $1/D$ dependence, while for needles $2 - \beta_m = 0.2$ giving a $D^{0.2}$ relationship. Since the bin model allows for the sublimation of the smallest crystals first, the spheres that have a $1/D$ growth relationship will loose larger concentrations than the $D^{0.2}$ relationship for needles. Thus, for a given percentage mass loss ratio (below about 0.50) the per-
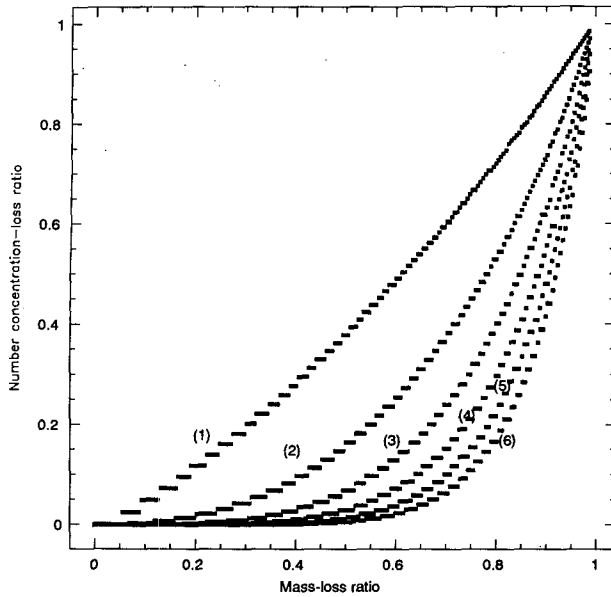
FIG. 6a. Evaporation ratio for varying ν: Curve 1 describes evaporation for $\nu = 1$, curve 2 describes evaporation for $\nu = 2$, up to $\nu = 6$. For these simulations $T = 273.15$ K, $P = 400$ mb, $\bar{D} = 30$ μm, and $S_i = 0.8$. Crystal habit: needles.
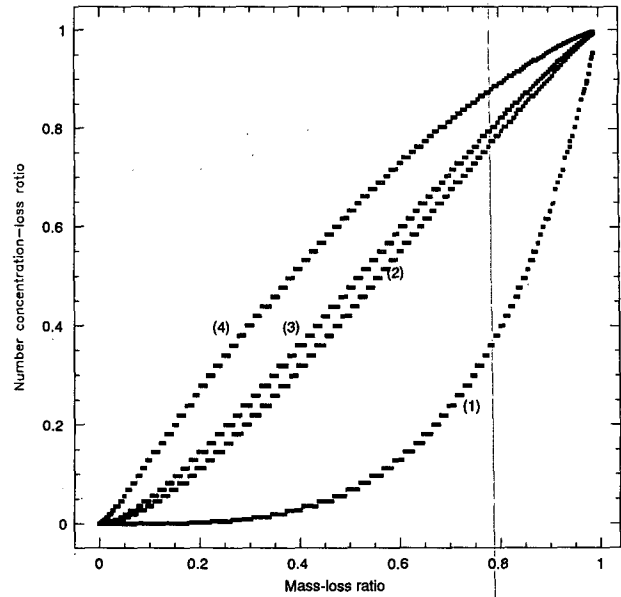
FIG. 6b. Evaporation ratio for varying crystal habit: Curve 1 describes evaporation for needles and for long columns, curve 2 for hexagonal plates, curve 3 for short columns, and curve 4 for spheres. Simulations T, P, S_i, and $\bar{D}$ are the same as above. A shape parameter of $\nu = 3$ used.

centage number concentration loss will be larger for the sphere than for the needle habit.

4. Tests using a Lagrangian parcel model

The evolution of the ice spectra is examined in this section with the use of a Lagrangian parcel model as described in Tripoli and Cotton (1981). The test model consists of the following general structure: the ice liquid water potential temperature θ_{il}, which is the model conservative variable; initial conditions that consist of the initial parcel temperature; the total parcel mixing ratio r_i; the model top and bottom (defined by two pressure levels); and an initial updraft profile.

The model is initiated with initial model top and bottom pressures, P_{top} and P_{bot}; an initial temperature T_0; and an initial total mixing ratio defined as

$$r_t = r_v + r_p + r_s, \tag{38}$$

where r_v is the mixing ratio of water vapor, r_p is the mixing ratio of pristine ice, and r_s is the mixing ratio of snow. A constant model ascent is assumed during simulations in order to isolate the transfer process. A model pressure increment ΔP is assumed and, using the hypsometric equation, it is possible to get a height scale ΔZ from the ΔP increment. This height increment and the model ascent are used simply as a way of estimating a model time step:

$$\Delta t = \frac{\Delta Z}{w}. \tag{39}$$

Model temperature at the given pressure level is diagnosed from the conservative variable θ_{il} as described in Tripoli and Cotton (1981). Since θ_{il} is conserved under phase changes of water but not for precipitating processes, we choose to allow all of the initial water species to travel with the parcel and not allow fluxes of any species into or out of the parcel.

Model ice is allowed to form through the heterogeneous, deposition/condensation freezing ice nucleation formulation of Meyers et al. (1992):

$$N_i = \exp\{a + b[100(S_i - 1)]\}, \tag{40}$$

where N_i is the number concentration nucleated (m^{-3}), S_i is the ambient saturation with respect to ice, and a and b are empirical constants derived from fits to nucleation data with $a = 0.639$ and $b = 12.96$ (mks).

In order to test the feasibility of our parameterization of the transfer processes and the sublimational number concentration loss schemes, we compare the parameterized processes to those calculated with a "bin resolving" methodology. This method is similar to the method illustrated in Fig. 4. We assume that the transfers and concentration losses calculated with this method are the "truth" and use the results as a comparison basis. We calculated the transfers using this method by dividing up the pristine ice (or snow) distribution into $N_b = 20\ 000$ bins of width ΔD with the bins remaining fixed in time. The spacing, ΔD, decreases as D_b and $D = 0$ are approached so that accurate calculations of the transfer processes and the sublima-

tional loss can be calculated. During ice crystal growth (sublimation) we can find the appropriate number concentration and mass mixing ratio that is transferred between the distributions by calculating the change in size and mass of the particles in each bin. As particles are grown, the bins in the region of D_b are checked to see if their sizes have increased beyond (below) D_b due to vapor growth (sublimation). If this condition is true, the concentration and mass associated with that bin are transferred to the snow (pristine ice) class. In the case where a fraction of a bin must be moved, the same procedure as was adopted in finding the sublimational concentration loss values is employed. For the case where the parcel is subsaturated with respect to ice, not only crystal transfers occur, but so do losses of concentration to vapor. In this case we invoke the same methodology as described above.

Model results

Simulations were conducted in which the ability of the above scheme could best be demonstrated against the bin-calculated transfers. The results presented here include variations in crystal habit and the shape parameter of the pristine ice distribution. Since crystal habit has a large influence on the growth and the transfer of crystals between distributions through its power formulation [Eq. (5)], the two crystal habits that characterize the maximum and minimum of the parameter β_m are used, which are needles, $\beta_m = 1.8$, and hexagonal plates, $\beta_m = 2.6$. These two types represent the extremes of crystal growth as a function of habit in the model. Tests have been conducted with other crystal types having values of the exponential parameter β_m intermediate to those stated above. The model results, expectedly, are intermediate to those that follow for needles and plates. The shape of the distribution ν also has a large influence over the behavior of the given system, and a model simulation in which different values of ν are used is discussed. Three cases comprise the results that follow: they are a case in which needle crystals are utilized with a shape parameter of $\nu = 3$ for the pristine ice distribution, a case in which needle crystals are utilized with a shape parameter of $\nu = 1$ for the pristine ice distribution, and a case in which hexagonal crystals are utilized with a shape parameter of $\nu = 1$. The snow distribution shape is held constant at $\nu = 3$ for all of the simulations.

1) CASE 1: NEEDLE CRYSTALS WITH PRISTINE ICE DISTRIBUTION SHAPE $\nu = 3$

Parcel ascent is initiated with enough water vapor ($r_v = 0.0008$ kg/kg) and at a sufficiently low temperature ($T = 243$ K) so that ice supersaturation is realized initially. A constant upward motion of $w = 1$ m s^{-1} is assumed, and this leads to a time step of $\Delta t = 1.77$ s. Figure 7 shows the profile of S_i during model ascent
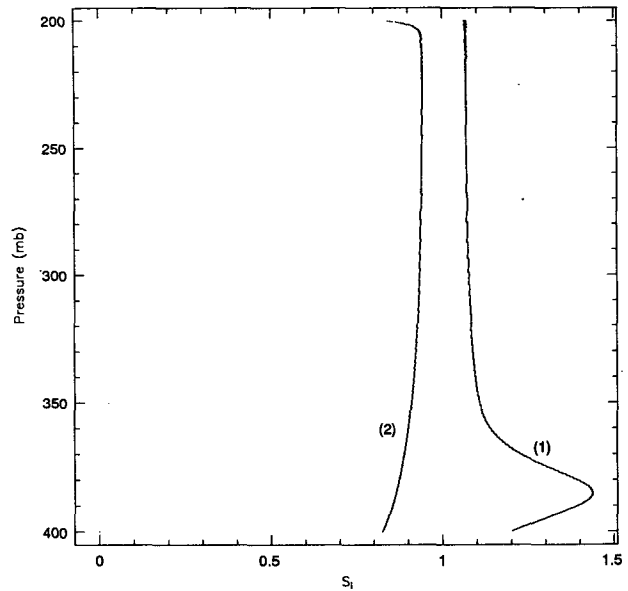

FIG. 7. Plot of S_i vs pressure for case 1: Model ascent and descent are denoted by curves 1 and 2, respectively.

and descent. Note that the ice supersaturation increases rather quickly due to adiabatic cooling. This increase is rapidly damped as the nucleated ice crystals grow by vapor deposition and deplete the vapor supply. For descent the parcel is initialized with a mixing ratio of vapor ($r_v = 0.00007$ kg/kg) that is low enough so that ice subsaturated conditions are initially realized. Profiles for both model ascent and descent reach approximate "equilibrium" values, thus sustaining constant growth (sublimation) of the model ice.

Figure 8 shows the evolution of the pristine ice (solid lines) and snow (dashed lines) spectra during the ice supersaturated ascent. The time for the full ascent from 400 to 200 mb is 2000 s with the time into the simulation of each of the plotted distributions indicated in the figure. Note that the initial pristine ice distribution is quite narrow, being associated with high number concentrations and low mass mixing ratios. This can be seen in Figs. 9a and 9b; note that the concentration peaks quickly because of the nucleation equation while the mass mixing ratio of the pristine ice crystals is small. The pristine ice distribution rapidly broadens to the distribution shown at $t = 171.69$ s, and after this time the change in the distribution of pristine ice is rather slow since the profile of S_i is decreasing. This may be seen by examining Fig. 9c in which the profiles of the mean particle sizes are plotted. The pristine ice profile (solid line) rapidly reaches the delineating size between pristine ice and snow (D_b), which is the bounding size of the pristine ice category. This emphasizes the rapid broadening of the pristine ice class.

This rapid increase in the mean size of the pristine ice distribution is explained as follows. First, the nu-
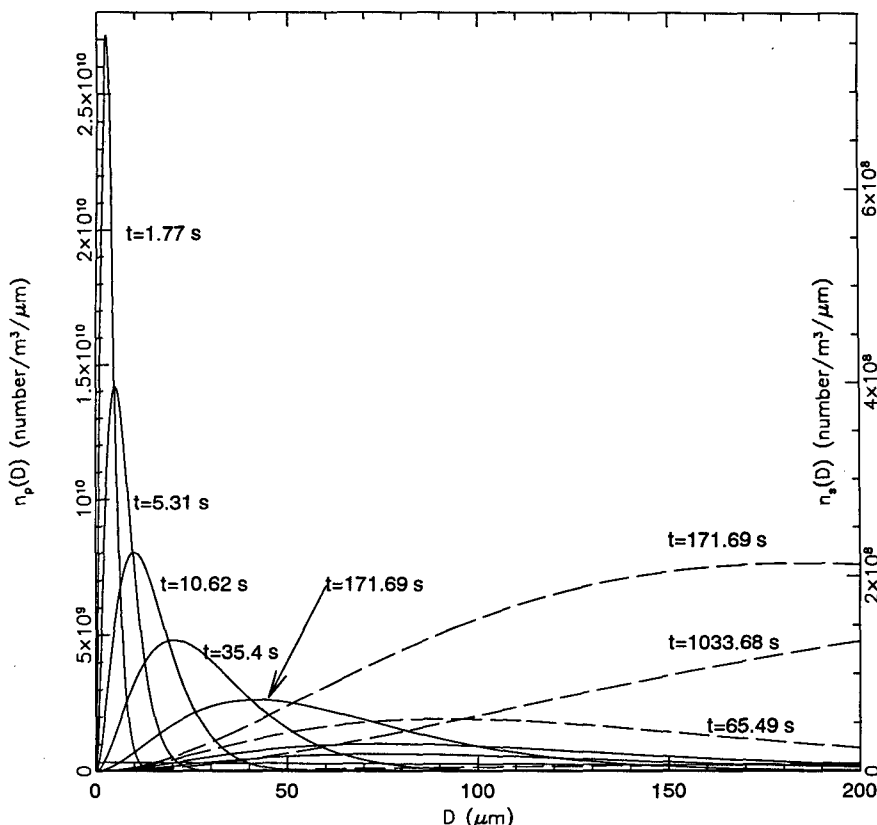
FIG. 8. Evolution of the ice spectra for case 1 during ascent. Pristine ice evolution is shown by the solid set of curves, and snow is shown by the dashed set. The times during the simulation that each spectrum was plotted is indicated near its respective distribution.

cleated particles are growing in a highly supersaturated environment. Note that the most rapid increase in size of the pristine ice particles occurs where S_i is increasing rapidly. These high values of S_i cause increased vapor depositional growth rates. The growth rate affects the maximum size of the ice particles in accordance with the mass dimensional relationships ($m = \alpha_m D^{\beta_m}$). The important parameter here is the value of β_m, which has a value of 1.8 for needle crystals. By examining Fig. 10a, one can see that for a given increase in mass there is a larger increase in maximum size than for, say, the ice sphere. The reason for this comparison is that we are generally more accustomed to thinking of the growth of spherical particles (drops, hailstones, etc.). Of course, this mass–dimensional relationship affects the growth rate of the particles. Figure 10b shows how this relation affects the growth of the major dimension of the crystal; note that this figure shows only how dD/dt varies with D and not how other variations affect growth. For needle crystals (solid line with $\beta_m = 1.8$) note that the growth rate increases with D. Contrasting this with the sphere (dot-dashed line with $\beta_m = 3.0$), one can see that, since the needle growth rate does not decrease quickly with size (as does the sphere), distribution broadening is facilitated.

Figure 9a, which shows the profiles of the total concentration of pristine ice (solid line) and snow (long dashed line) for model ascent, illustrates the parameterized transfer process developed above. Note that the pristine ice distribution initially peaks quickly due to the high supersaturations during the initial stages of the ascent. At these stages transfer of concentration to snow begins. This halts the increase in pristine ice concentration as the increasing growth rates causes large concentration transfers to snow. The profile of the concentration transfer to snow (solid line) is shown in Fig. 11a, and, as we expect, transfer rates are highest in the first few millibars of the ascent because of the peak in the S_i profile. The transfer profile drops rapidly with the profile of S_i, as we expect. The crosses plotted in Fig. 11a are the transfers calculated with the bin model. Note that there is quite good agreement between the analytical calculations of transfer rates and the bin calculations, which gives us confidence in our method. Near $t = 500$ s the bin calculations become discontinuous; this is because the bin method has discrete size boundaries. This can be made less discontinuous by increasing the bin resolution; however, the increment used is good enough to illustrate the agreement.
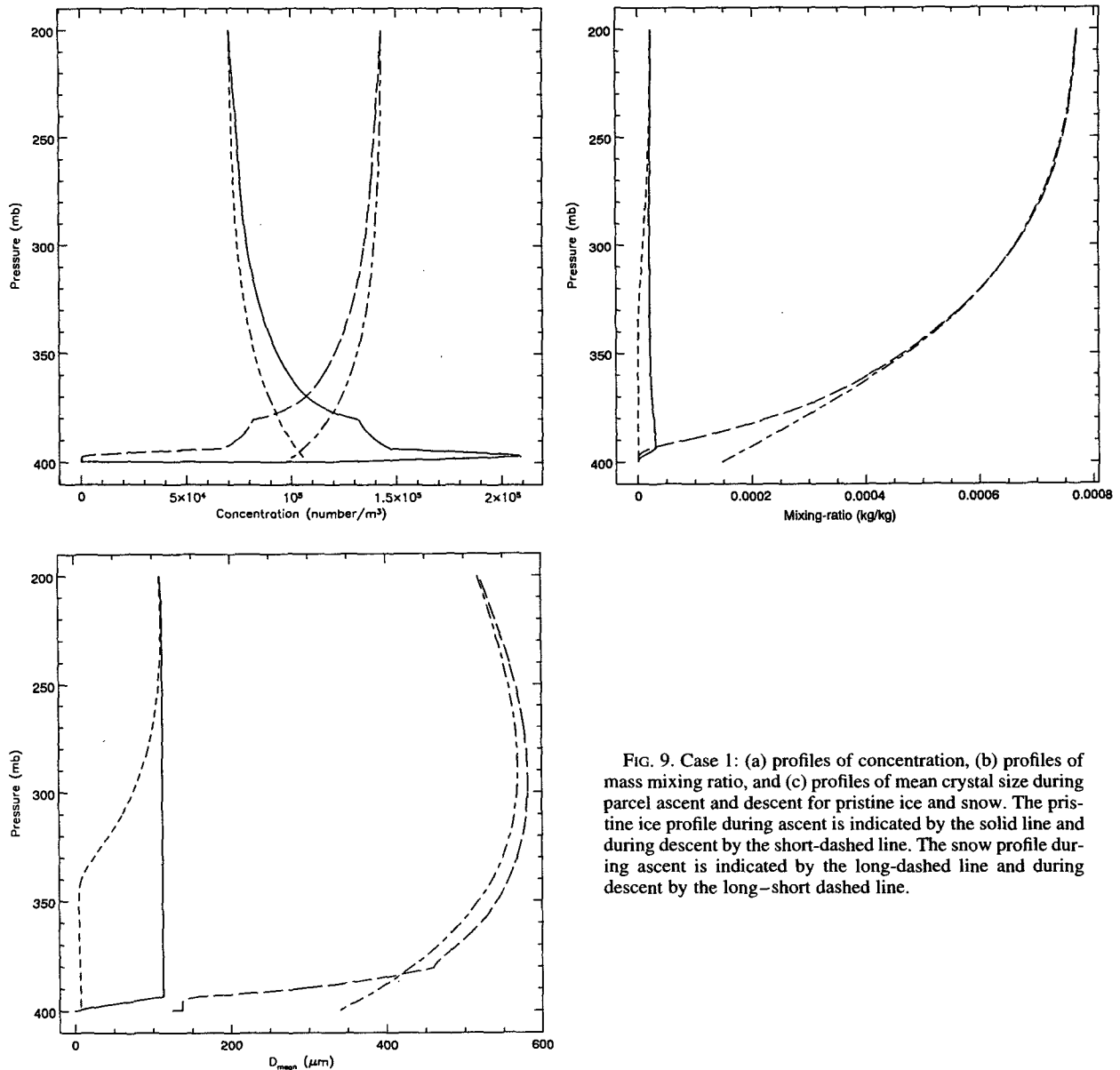
FIG. 9. Case 1: (a) profiles of concentration, (b) profiles of mass mixing ratio, and (c) profiles of mean crystal size during parcel ascent and descent for pristine ice and snow. The pristine ice profile during ascent is indicated by the solid line and during descent by the short-dashed line. The snow profile during ascent is indicated by the long-dashed line and during descent by the long–short dashed line.

The profile of mass mixing ratio as shown in Fig. 9b for pristine ice has qualitatively the same physical explanations as the number concentration profiles discussed above. There is an initial peak in the mass mixing ratio for pristine ice due to the initial spike in number concentration. This profile drops off as mass mixing ratio is transferred to the snow distribution by the analytical transfer equations (Fig. 11b, solid line). Again, the transferred mass profile follows closely the S_i profile. Note the correspondence between the analytical method and the bin method. Error analysis between the two was performed by calculating the percent error between the analytical method and the bin method, which

was subsequently averaged. The error in these calculations was rarely over 10%, and the average was below 1% for both the number and mass transfers.

The snow distribution is plotted in Fig. 8 and is shown for the times $t = 65.49$, 171.69, and 1033.68 s in order to illustrate its evolution. The snow distribution, like the pristine ice distribution, broadens rather quickly during the initial stages of the ascent (first 30 mb) due to the high supersaturations. This is also detectable in Fig. 9c, which shows the rapid increase in the mean snow size during the ascent. Note that in Figs. 9a and 9b we see that the concentration of snow levels off rather rapidly after the profile in S_i drops off since
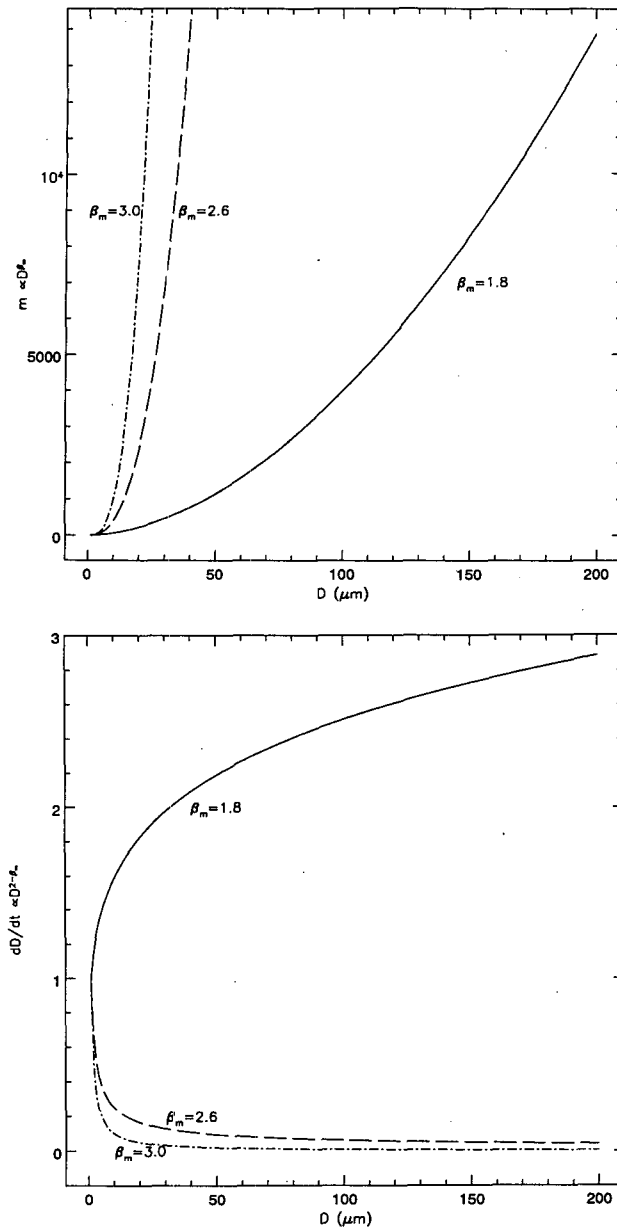
FIG. 10. (a) Mass–dimensional relationships for different values of β_m. (b) Growth rate dependence on crystalline maximum dimension, D, and β_m.

the transfer of pristine ice concentration is the only source of snow concentration. However, the mass mixing ratio of snow continually increases because it is supplied not only by the transfer process but also by vapor deposition. One can imagine that, if transfer of pristine ice mass and concentration dominated the snow mass source, then snow mean sizes should not increase as quickly since the mass and concentration transferred are associated with smaller sizes (about 125 μm). Vapor growth can cause such increases in the mean size

because of the influence of the power β_m in the mass–dimensional relationship. As stated above, a given amount of mass distributed over the needle crystal will cause a greater increase in the maximum size as compared to a sphere. This relation thus has an influence on how the vapor growth equation "levels off" and how this, then, affects distribution breadth. Figure 10b shows how the mass–dimensional relationships affect the increase in maximum particle size. Note that for the sphere ($m \propto D^3$) the growth rate drops off rapidly with size. For the needle crystals, however, this is not the case: the growth rate initially increases rapidly; however, this increase drops off with size. This is the reason for the point at which the snow distribution reaches a maximum mean size (of about 580 μm) in Fig. 9c. Note that the maximum mean size of the snow crystals in Fig. 9c begins to decrease after the 300-mb level is reached. This shows the distribution narrowing caused by smaller crystals whose maximum dimensions are growing faster than the larger particles coupled with the addition of more smaller particles from the pristine ice distribution.

The model subsaturated descent follows a similar analysis. The distributions for model descent are not plotted; however, all of the pertinent information can be found in the figures of the mean particle size, number concentration, and mass mixing ratio profiles. Examining the profiles of the mean sizes of pristine ice (short-dashed line) and snow (long-short dashed line) in Fig. 9c, two things can be duly noted. First, the size of the pristine ice particles falls off slowly, indicating the narrowing of the pristine ice distribution. Second, the mean size of the snow crystals first increases and then decreases during the ice subsaturated descent indicating broadening and then narrowing of the distribution. The pristine ice mean crystal sizes decrease because, as can be noted by comparing Figs. 9a and 9b, the concentration of pristine ice is increasing while the mass mixing ratio is decreasing due to sublimation. The concentration increase of pristine ice is due to the fact that the transfer of concentration from the snow distribution to the pristine ice distribution is larger than the sublimational loss of concentration (which is shown in Fig. 12). Mass mixing ratio loss through sublimation is larger for the pristine ice distribution than is the addition of mass from the snow distribution. Thus, we have larger concentration with decreasing mass mixing ratio leading to smaller sizes. Note that the sublimational concentration loss plotted in Fig. 12 increases toward the end of the model descent. This goes along with Fig. 5a, which shows that large ratios of the sublimation rate to the total mixing ratio are needed for ν = 3 distributions before significant concentration will be depleted. Obviously, this will only occur when the distribution is very narrow and not much mass is associated with the pristine ice crystals. Also plotted in Fig. 12 are the calculations of concentration loss due to sublimation with the bin methodology (represented
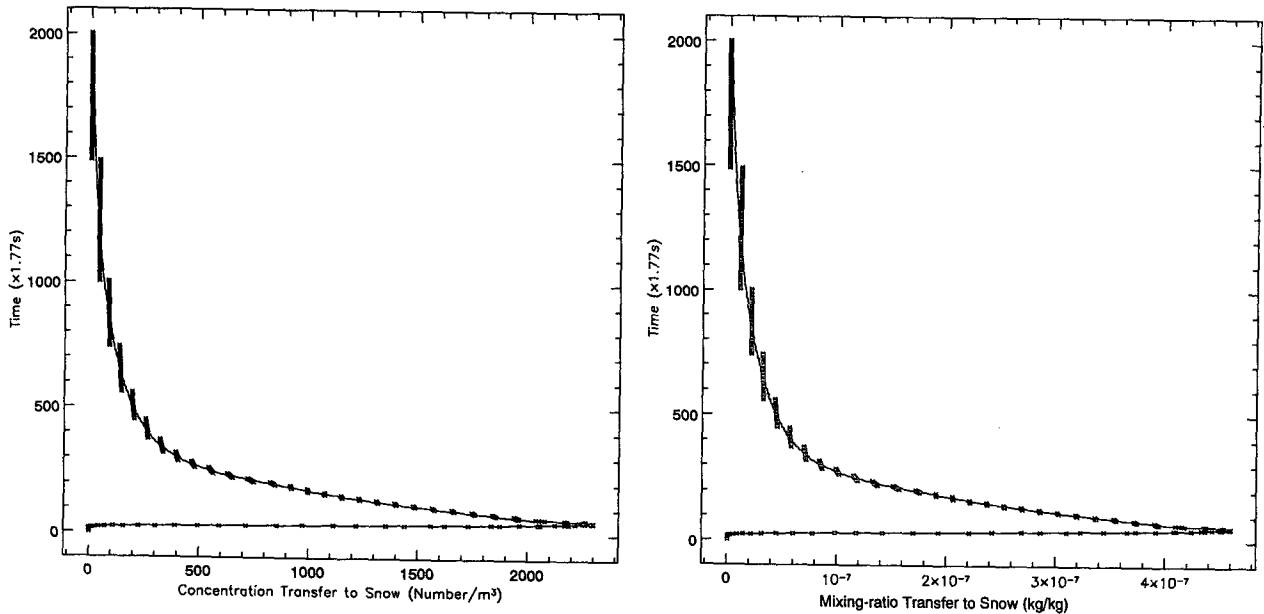
Fig. 11. Case 1: (a) concentrations transferred to snow at each pressure level and (b) while mass mixing ratio transferred to snow at each pressure level during parcel ascent. The solid line indicates the model parameterization results, while the crosses indicate the bin model calculations.

by the solid line). The parameterized sublimational loss of number concentration (crosses) follows the shape of the bin-calculated profile (solid line) well with some deviation that is due to the increment of mixing ratio stored in the tables (recall we used 2%). Error associated with this parameterization reach maximums
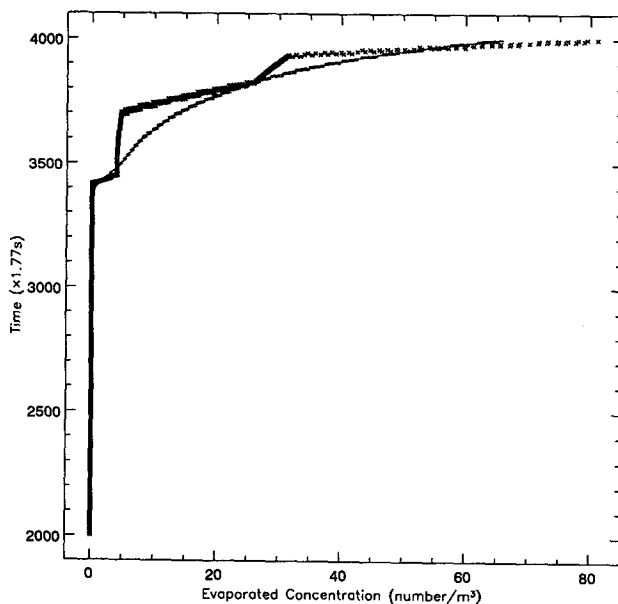

Fig. 12. Sublimational concentration loss during parcel descent for case 1. The crosses indicate the parameterized results, while the solid line indicates the bin model results.

of about 48% with an error averaged over the entire descent of about 10%.

For the snow distribution, initially during the descent, concentration transfer to snow is greater than the amount of mass mixing ratio lost to vapor or to pristine ice through transfer; therefore, initially, mean snow sizes increase. Once the 300-mb level is reached, however, the mean size of the snow crystals begins to decrease because the increase in the mass mixing ratio loss to vapor and to pristine ice through transfer is overcoming the transfer of snow crystal concentration to pristine ice.

2) Case 2: Needles with pristine ice distribution shape $\nu = 1$

Figure 13 is a plot of the evolution of the pristine ice (solid lines) and the snow (dashed lines) distributions during model ascent; times are indicated on the figure for reference. Here, even though the distribution shape of the pristine ice category has been chosen to be $\nu = 1$ to conform more with observations of the spectral shape of small ice distributions, the evolution of the spectra is similar to that given above. The pristine ice distribution quickly broadens due again to growth in a largely supersaturated region (see Fig. 7) and due to the sensitivity of vapor growth to the β_m parameter in the mass–dimensional relationship. Again, we see an initial peak in the pristine ice number concentration profile (Fig. 14a) followed by a rapid drop in pristine ice concentration due to the fact that nucleation is limited by the number of crystals present and that concen-
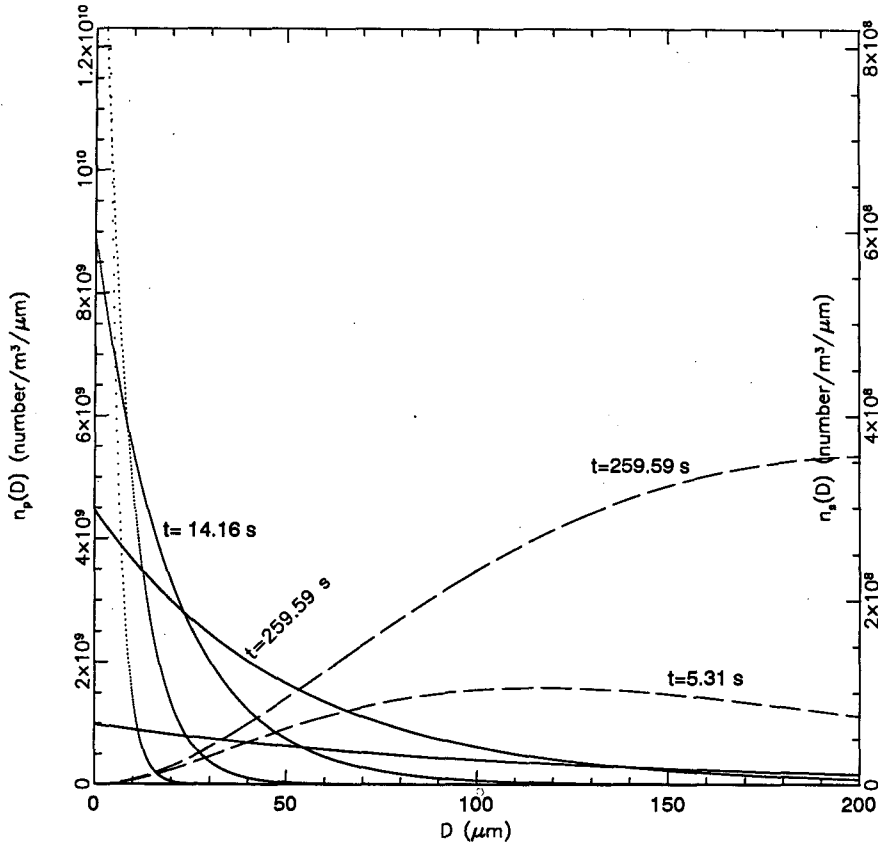
FIG. 13. Evolution of the ice spectra during parcel ascent for case 2.
The same curve delineations are used as in Fig. 8.

tration is being quickly transferred to the snow category (see Fig. 15a). The mass mixing ratio profile for pristine ice during model ascent shown in Fig. 14b (solid line) shows the same trends as those in the previous section. The profiles of the mean particle sizes for the pristine ice (solid line) and snow (long-dashed line) categories during model ascent also show these similar trends. Note that the snow category reaches smaller mean distribution sizes during the evolution; this is definitely due to the fact that the transfer of concentration and mass mixing ratio are from a differently shaped pristine ice spectra. Figures 15a and 15b show the model-parameterized transfers of number concentration and mass mixing ratio, respectively, as compared to the bin calculations (crosses). Once again, the agreement between the parameterization and the more accurate bin model are in quite close agreement with errors the same as given in the previous section.

The main difference between the above simulation and the one presented in this section is in the descent profiles. Figure 14c shows the evolution of the pristine ice (short-dashed line) and the snow (long–short dashed line) mean distribution sizes during the ice subsaturated descent. We note the same features as discussed in the previous section with the mean pristine ice sizes decreasing during descent showing distribution narrowing and the snow distribution mean crystal size first increasing and then subsequently decreasing as descent continues. As before, the pristine ice category is losing more mass to vapor than concentration since there are significant numbers of pristine ice crystals associated with the larger, more massive sizes. This is confirmed by examining Fig. 16, which shows the concentration loss to sublimation (parameterization results are the crosses). Initially, the concentration loss is low since sublimation rates are a very small fraction of the total distribution mass. Toward the end of the descent, however, the pristine ice mean distribution size again begins to increase. Note that this increase corresponds to the approximate point in Fig. 16 where the concentration loss to sublimation begins to dip. This increase also corresponds to the point where the snow concentration begins to decrease more rapidly; this point is at about 370 mb (short-long dashed line) in Fig. 14a. This shows that snow concentration and mass mixing ratio transfers to pristine ice are increasing, thus, adding significant large (about 125 μm) crystals to the pristine ice distribution. Of course, this will tend
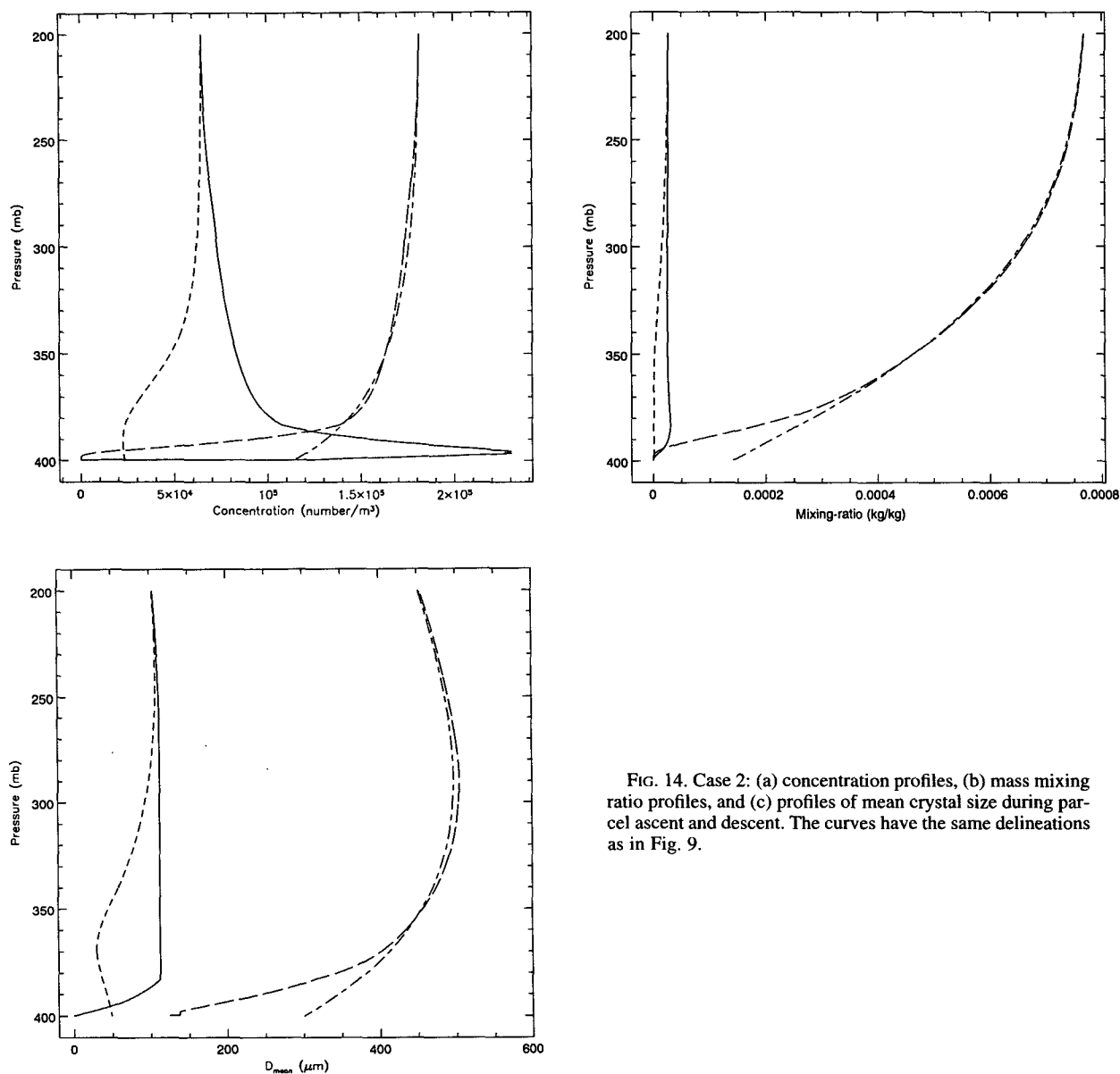
FIG. 14. Case 2: (a) concentration profiles, (b) mass mixing ratio profiles, and (c) profiles of mean crystal size during parcel ascent and descent. The curves have the same delineations as in Fig. 9.

to increase the mean size of the pristine ice distribution. This increased mass of pristine ice results in smaller ratios of sublimation rates to total distribution mass and is the reason that the dip in the sublimational loss profile occurs where it does.

The sublimational concentration loss profile given in Fig. 16 shows how the parameterized concentration losses compare to accurate calculations using the bin-resolving model (solid line). Note that the shapes of the profiles are distinctly similar with some significant deviations. Here, differences between the parameterization and the bin model were somewhat less with maximum error of 42% and error averaged over the whole descent of only 5%.

3) CASE 3: HEXAGONAL PLATES WITH PRISTINE ICE DISTRIBUTION SHAPE, $\nu = 1$

The evolution of the ice spectra during model ascent is plotted in Fig. 17, with times indicated on the figure. Again, both distributions, pristine ice (solid line) and snow (dashed line), broaden due to vapor depositional growth. Note, however, that in this case the distributions broaden more slowly than the needle cases presented previously; by $t = 309.75$ s, neither distribution has broadened significantly. This fact is also elucidated in Fig. 18a where the evolution of the mean particle sizes of pristine ice (solid line) and snow (long-dashed line) during model ascent are shown. The pristine ice
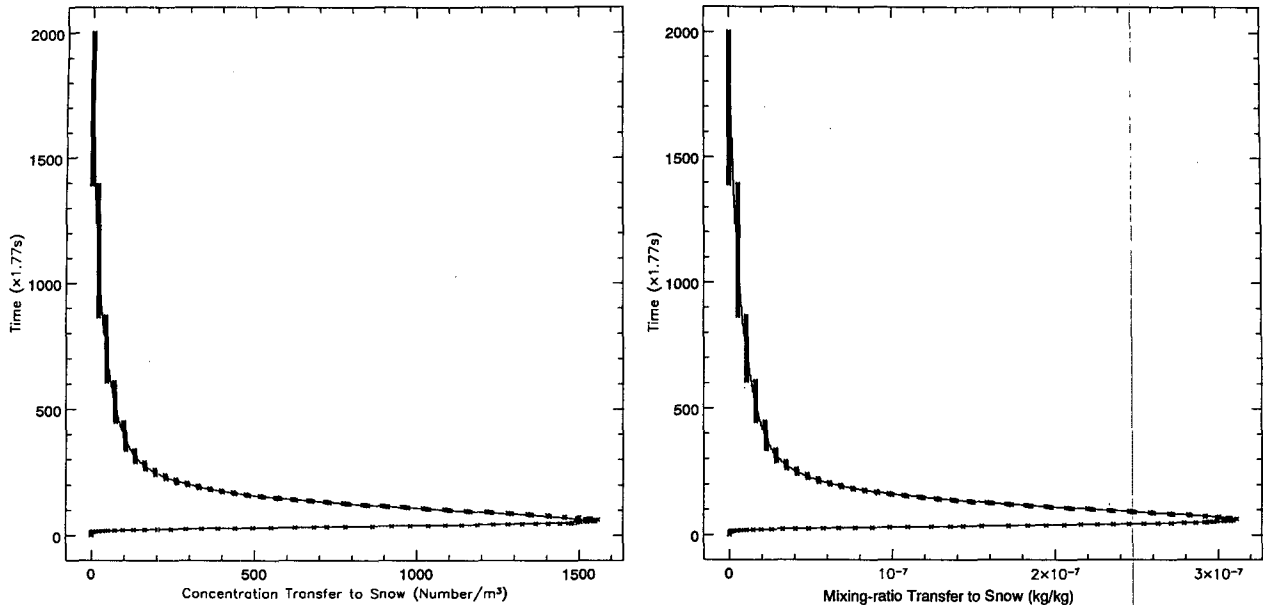
FIG. 15. Case 2: (a) concentration transferred to snow and (b) mass mixing ratio transferred to snow
at each pressure during parcel ascent. The curves have the same delineations as in Fig. 15.

mean size increases slowly however; it never reaches its maximum size of 125 μm throughout the duration of the ascent. The pristine ice distribution, thus, remains quite narrow. The snow distribution shows similar behavior, with very slow increases in the mean size of the crystals during the initial stages of the ascent and then some narrowing (decrease in the mean size) above

about 365 mb. The initial increase in distribution breadth is due to the growth of particles by vapor deposition in the highly ice supersaturated portion of the ascent (see S_i profile). The later narrowing is due to slowed growth rates of the larger particles and the addition of smaller particles from the pristine ice distribution through the transfer process.

The reason for lesser broadening of the distributions in comparison to the needle cases presented previously
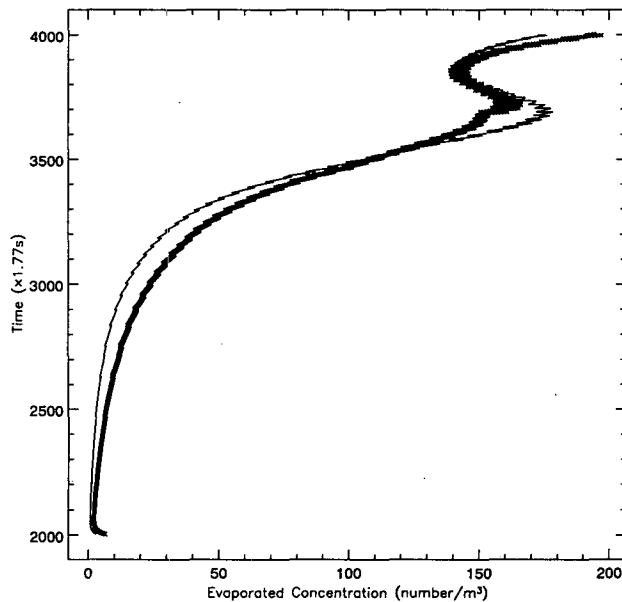

FIG. 16. Sublimational concentration loss during model ascent for case 2. The crosses indicate the model parameterization, while the solid line indicates the bin model calculations.
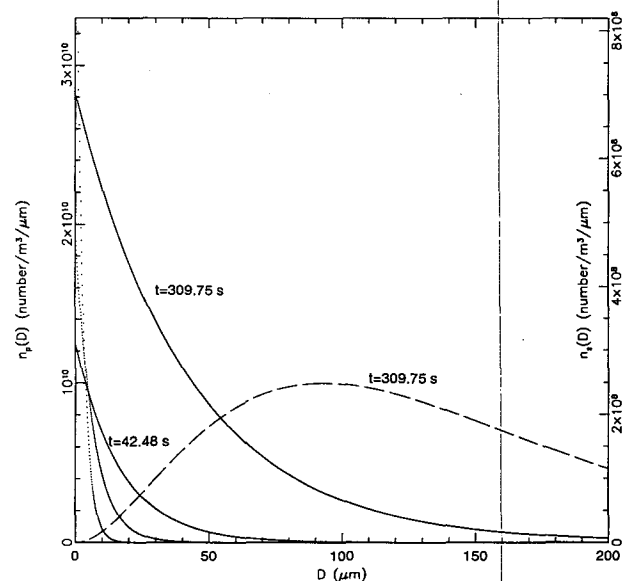

FIG. 17. Evolution of the pristine ice and snow spectra during model ascent. The curves are delineated as in Fig. 8.
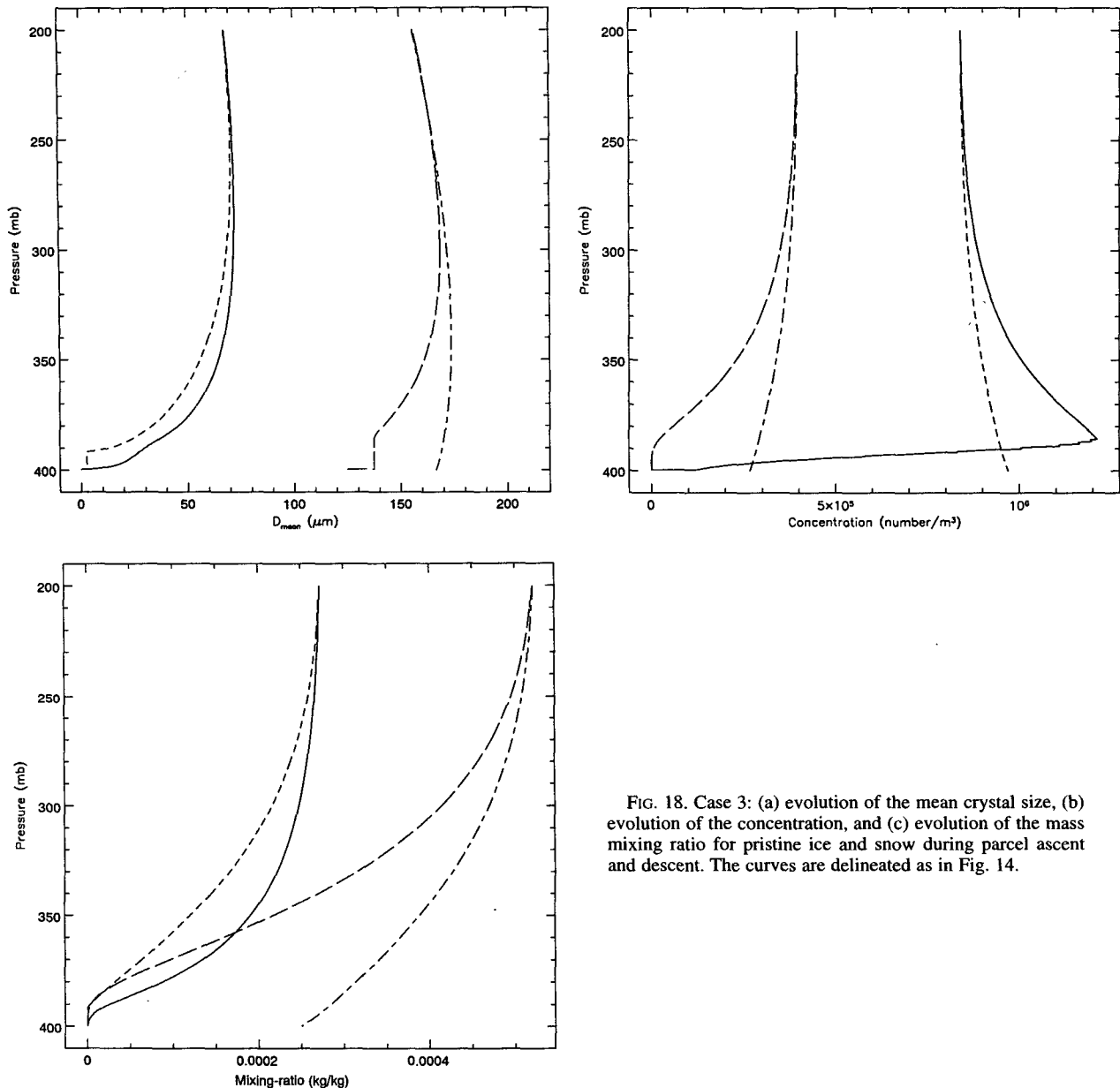
FIG. 18. Case 3: (a) evolution of the mean crystal size, (b) evolution of the concentration, and (c) evolution of the mass mixing ratio for pristine ice and snow during parcel ascent and descent. The curves are delineated as in Fig. 14.

is related to the mass–dimensional relationships used for the hexagonal plates. For hexagonal plates the β_m parameter is 2.6 and, as is shown in Fig. 10a, for these particles as D increases, additional mass added to the particle will affect D less when compared to the case of needle crystals. This, therefore, is the reason for the lessened broadening in comparison to the needle case. The reduced broadening can also be explained in terms of Fig. 10b; note that here the effect of the mass–dimensional relationship on the growth rate is plotted. For the needle case higher growth rates are realized; however, for the hexagonal plate and the sphere the growth rate drops off rapidly with size.

Because of differences in growth rates facilitated by the mass–dimensional relationship and differences in the capacitance term, less vapor is deposited on the hexagonal plates than was on the needle crystals. This is due mostly to the much smaller sizes of the hexagonal plates. As a result of this, less vapor is removed from the parcel in the highly ice supersaturated portion of the ascent and, therefore, more nucleation can take place. This is shown in Fig. 18b where it can be seen that the profile of the concentration of pristine ice during the model ascent (solid line) continues to increase for a short time. Compare this to the needle case where the pristine ice profile sharply decreased after peaking.

Note that the snow concentration profile during model ascent (long-dashed line) increases very slowly. This is because the transfer rate of concentration from the pristine ice category is slow. This slow transfer to snow is due to the narrow pristine ice spectrum and because dD/dt, as shown in Fig. 10b, is quite small in the region of 125 μm where the transfer is occurring. Figure 19a shows this slow transfer process; note that fewer crystals are transferred to the snow distribution in this case than in the case of needle crystals.

Another consequence of the mass–dimensional relationship is its effect on the profiles of mass mixing ratio. Figure 18c shows the profiles of pristine ice (solid line) and snow (long-dashed line) during model ascent. Because deposition of mass affects D less in the case of hexagonal plates in comparison to needles, more mass can be deposited on the pristine ice distribution without increasing transfer to the snow category. The mass mixing ratio profile shows this; note that the profile of mass mixing ratio for the pristine ice class has much higher values than did the previous needle cases. This is also illustrated in Fig. 19b, which as in the case of number transfer shows smaller mass mixing ratio transfers for hexagonal plates than for the needle cases when compared to the results presented in the previous section.

Once again, bin model calculations of the transfers of concentration and mass mixing ratio were calculated and compared to the parameterized results. Examining Figs. 19a and 19b, one can easily see that there is good agreement between the parameterization (solid line) and the bin model calculations (crosses). Again, there are some discontinuities in the profile calculated with the bin model that have to do with the specific size delineation inherent in bin models. Errors here were as large as 12% with errors averaged over the whole ascent of about 3%.

The model-induced ice subsaturated descent shows similar features to those presented in previous sections of this paper. The mean size of the pristine ice crystals (short-dashed line in Fig. 18a) remains close to constant during approximately the first half of the descent (until about 300 mb) and then decreases, exhibiting the narrowing of the pristine ice distribution. Figure 20 shows the profile of the concentration lost to sublimation (crosses) from the pristine ice distribution. This is partially the reason for the constant mean particle sizes during the initial portions of model descent. During the initial descent, the concentration lost to sublimation is largest (since dD/dt increases rapidly as D decreases, see Fig. 10b); however, at this time larger particles are being added from the snow distribution during the largest-ice subsaturations. These larger particles tend to offset the loss of concentration, and thus smaller sizes, from the distribution keeping the mean pristine ice sizes fairly constant. As the bottom of the descent is approached (400 mb), note that in Fig. 18b the pristine ice concentration (short-dashed line) is increasing

while, as is shown in Fig. 18c, the mass mixing ratio of the pristine ice category (short-dashed line) continually decreases. This causes the mean particle size of the pristine ice category to decrease; thus the distribution narrows. The reason for the increase in concentration near the bottom of the model descent is increased transfer rates of concentration from the snow category that cannot be offset by sublimational concentration losses (as shown in Fig. 20, this is too small).

Figure 20 compares the parameterized concentration loss (crosses) to the more accurate bin model calculations (solid line). Note that, again, the profile shapes are similar; however, the numbers are not exactly similar. Errors here became as large as 70%, with errors averaged over the entire descent reaching values of 13%.

The mean size of the snow category (long-short dashed line in Fig. 18a) increases throughout a large portion of the descent until the parcel is below about 350 mb where the mean size begins to decrease. The initial increase in mean size is due to a slower decline in mass mixing ratio (as shown in Fig. 18c, short-long dashed line) in comparison to concentration transfer to pristine ice. The loss of the smaller snow particles to pristine ice during transfer causes the larger crystals in the snow distribution to be weighted more, thus the increase in mean size. After the 350-mb level has been reached the snow category begins to lose mass more rapidly (because of the increase in dD/dt with decreases in D). When this occurs, the snow particles rapidly decrease in size and the distribution narrows.

5. Summary and conclusions

In this paper we have presented an analytical method for describing ice crystal transfer processes due to vapor depositional growth with a complete gamma distribution representation when predicting on two moments of the ice hydrometeor spectra. Equations were developed that describe the transfer of pristine ice to snow when ambient conditions are ice supersaturated and for the transfer of snow to pristine ice when ambient conditions are ice subsaturated. Since ice crystal number concentration "buildup" occurs during ice subsaturated conditions, a parameterization of a number concentration sink was described in which the fractional number concentration loss is tabulated as a function of the fractional mass mixing ratio loss, the shape of the distribution ν, and the habit of the ice crystal.

Tests of this scheme were accomplished using a Lagrangian parcel model described in Tripoli and Cotton (1981). The model allowed for the testing of the parameterizations via comparison to fluxes and sublimational concentration losses calculated with a bin-resolving model. The parameterization showed significant sensitivity to both the value of the distribution shape parameter assumed (ν) and especially to the choice of crystalline habit (β_m variation). When needle
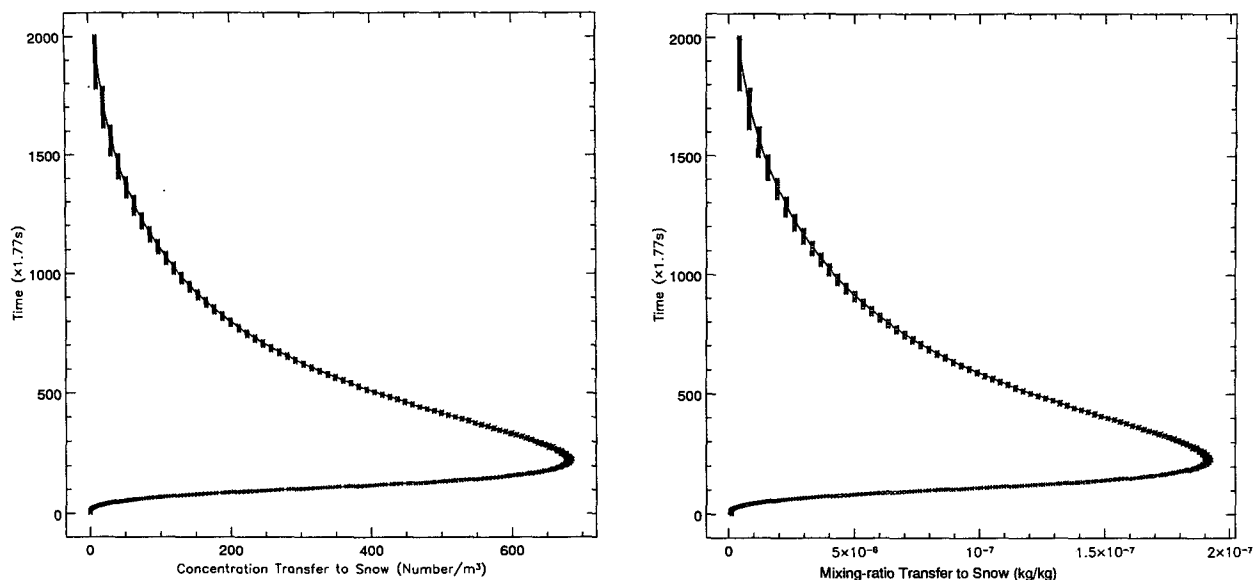
FIG. 19. Case 3: (a) transfer of concentration to snow and (b) transfer of mass mixing ratio to snow during parcel ascent. The curves have the same delineations as in Fig. 15.

crystals are utilized in the model, the pristine ice and snow size spectra broaden rapidly. This is a result of the mass–dimensional relationship for needle crystals, which allows the vapor depositional growth to affect the maximum dimension of the crystals largely in comparison to ice spheres. In comparison, hexagonal plates can be expected to be more narrow with larger concen-
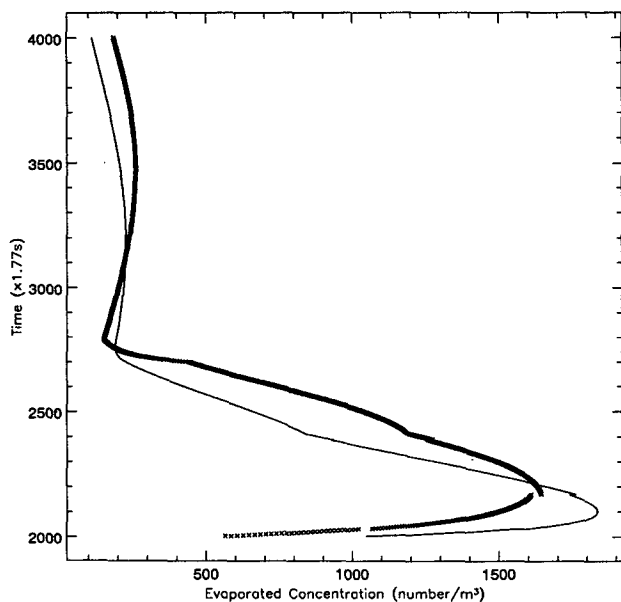

FIG. 20. Sublimational concentration loss profiles. The crosses indicate the parameterized calculations, while the solid line indicates the bin model calculations.

trations and mass mixing ratios associated with the pristine ice spectrum, while the snow category will contain much less mass and concentration in comparison to the needle case. The mean sizes of the crystals in the distributions are greatly affected by the mass–dimensional relationship through the vapor depositional growth equation. Because of this relationship, needle crystals can be expected to grow larger at a higher rate than the plate crystals. This facilitates the broadening of the pristine ice and snow spectra that are made up of needles. For the case of hexagonal plates the mass–dimensional relationship shows that these crystals behave more closely in a dimensional sense to spheres than to needles. Therefore, the distributions do not broaden much, staying narrow with larger concentrations and mass mixing ratios of pristine ice in comparison to the needle cases.

In general, the derived analytical expressions did very well in simulating the transfer process. The parameterizations showed similar transfer profiles to those calculated with a bin model, having maximum errors around 13% and errors averaged over the entire ascent of no greater than 5% with similar errors for the case of model descent. The sublimational number concentration loss parameterization compared less favorably to the bin model calculations than the flux parameterization. This is due to the simplification of this process, allowing sublimational concentration loss to be only a function of the shape parameter ν and the ratio of mass loss to vapor to total distribution mass. The model parameterization of sublimational concentration loss produced the shape of the bin model profile fairly well; however, there were some significant errors as-

sociated with the parameterizations deviation from the bin profile. Errors for some points could be as high as 70%, with most errors being around 10%.

This parameterization scheme is a part of the new RAMS two-moment microphysical module described by Meyers (1995). The new microphysical module allows for the prediction of concentration and mass mixing ratio of the hydrometeor species. Part II of this paper contains simulations of the 26 November 1991 FIRE II cirrus case with this new microphysical module and comparisons of the results to significant lidar and aircraft data taken on that day.

APPENDIX A

Derivation of the Mass Growth Equation

Differentiating (2) with respect to time gives us

$$\dot{r} = \frac{1}{\rho_a} \int_0^\infty \left(\frac{\partial m(D)}{\partial t} n(D) + m(D) \frac{\partial n(D)}{\partial t} \right) dD.$$
(A1)

Since this is in Eulerian form (i.e., distribution relative), the term $\partial m(D)/\partial t = 0$. For vapor depositional growth only the change in the spectra can be written

$$\frac{\partial n(D)}{\partial t} = -\frac{\partial}{\partial D} \left\{ \frac{dD}{dt} n(D) \right\},$$
(A2)

which gives upon substitution into Eq. (6),

$$\dot{r} = -\frac{1}{\rho_a} \int_0^\infty m(D) \frac{\partial}{\partial D} \left(\frac{dD}{dt} n(D) \right) dD.$$
(A3)

This may be written

$$\dot{r} = -\frac{1}{\rho_a} \int_0^\infty \frac{\partial}{\partial D} \left(m(D) \frac{dD}{dt} n(D) \right) dD$$

$$+ \frac{1}{\rho_a} \int_0^\infty \frac{\partial m(D)}{\partial D} \frac{dD}{dt} n(D) dD.$$
(A4)

The first term in (A4) goes to zero, which can be seen by writing it as

$$-\frac{1}{\rho_a} \int_0^\infty \frac{\partial}{\partial D} \left(m(D) \frac{dD}{dt} n(D) \right) dD$$

$$= \lim_{D \to 0} \left(m(D) \frac{dD}{dt} n(D) \right)$$

$$- \lim_{D \to \infty} \left(m(D) \frac{dD}{dt} n(D) \right).$$
(A5)

The function that we are taking the limit of can be written as

$$m(D) \frac{dD}{dt} n(D)$$

$$= \alpha_m D^{\beta_m} \Phi D^{2-\beta_m} \frac{N_t}{\Gamma(\nu)} \left(\frac{D}{D_n} \right)^{\nu-1} \frac{1}{D_n} \exp\left(-\frac{D}{D_n} \right)$$

$$= (\text{const}) D^{\nu+1} \exp\left(-\frac{D}{D_n} \right),$$
(A6)

in which we have used the relation $dD/dt = \Phi D^{2-\beta}$; right now we need only the D dependence, so do not be alarmed if we do not define Φ at this stage, as this will be done later in this section. The limit as $D \to 0$ of this function is zero, so is the limit as $D \to \infty$ since $\exp(-D/D_n)$ goes to zero faster than $D^{\nu+1}$ goes to infinity as long as ν is finite. The second term in (A4) alone constitutes $\dot{r}$:

$$\dot{r} = \frac{1}{\rho_a} \int_0^\infty \frac{\partial m(D)}{\partial D} \frac{dD}{dt} n(D) dD.$$
(A7)

Since

$$\frac{\partial m(D)}{\partial D} = \alpha_m \beta_m D^{\beta-1},$$
(A8)

we can write

$$\frac{\partial m(D)}{\partial D} \frac{dD}{dt} = \alpha_m \beta_m D^{\beta-1} \frac{dD}{dt} = \frac{dm}{dt},$$
(A9)

and thus Eq. (A7) becomes

$$\dot{r} = \frac{1}{\rho_a} \int_0^\infty \frac{dm}{dt} n(D) dD.$$
(A10)

APPENDIX B

Crystal Capacitance

Recall that we had written the capacitance term as

$$C_i(c, a) = \chi(A)D,$$
(B1)

where $\chi(A)$ is a function purely of the crystalline aspect ratio. The capacitance terms of all of the crystals that we are interested in can be written in this manner. To see this, we write down the capacitance relations:

$$C_i = \frac{c}{\ln(4c^2/a^2)}, \quad \text{needles}$$

$$C_i = \frac{ce}{\ln\left|\dfrac{1+e}{1-e}\right|}, \quad \text{columns}$$

$$C_i = \frac{ce}{2 \sin^{-1}(e)}, \quad \text{hexagonal plates}$$

$$C_i = \frac{c}{\pi}, \quad \text{thin plates}$$

$$C_i = \frac{c}{2}, \quad \text{ice spheres} \tag{B2}$$

where

$$e = (1 - a^2/c^2)^{1/2}. \tag{B3}$$

By examining each of the above capacitance relations, it becomes obvious that the capacitance terms can be written as a function of the given crystals aspect ratio multiplied by the length of its maximum dimension. For example, C_i for needles becomes

$$C_i = \frac{c}{\ln(4A)} = \chi(A)c = \chi(A)D, \tag{B4}$$

where

$$\chi(A) = \frac{1}{\ln(4A)}. \tag{B5}$$

Obviously, assuming that $\chi(A) = \text{const}$ is not a good approximation since A varies across the distribution. In a bulk model, however, it would add additional unwanted computational expense to store a and c values over ranges of D. Our way to compensate for this somewhat is to calculate bulk values of A depending upon how $\bar{D}$ (or $\bar{c}$) changes in a time step. This is done by approximating the mass of a crystal with roughly equivalent volumes as is shown below.

The capacitance term in the vapor depositional growth equation is accounted for by equating equivalent volumes to the mass maximum length relation given by (5). For needles we may approximate crystal masses in the following manner:

$$m = \rho_i V_i = \rho_i \frac{4}{3} \pi a c^2 \tag{B6}$$

where ρ_i is the bulk ice density, a is the minor axis and c (D) is the major axis, and V_i is the volume of an ellipsoid. Substituting (5) into (A6) and rearranging gives an equation for a in terms of c:

$$a = \left(\frac{3\alpha_m}{4\rho_i \pi}\right)^{1/2} c^{\beta_m - 2}, \tag{B7}$$

where D in (5) has been replaced by c.

When hexagonal plates are considered, the mass of the crystal may be written as

$$m = V\rho_i; \quad V = (0.649)c^2 a$$

$$= \rho_i (0.649)c^2 a, \tag{B8}$$

where V is found by considering the geometry of the face of a hexagon. Substitution of (5) into the above and rearrangement gives the minor axis a as

$$a = \frac{\alpha_m}{\rho_i (0.649)} c^{(\beta_m - 2)}. \tag{B9}$$

Using these formulas, bulk aspect ratios are calculated for a given distribution of pristine ice crystals or snow by using the mean crystal size $\bar{D} = \bar{c}$ and either (A7) or (A9) above to calculate a. The aspect ratio $A = c/a$ is recalculated from these values.

APPENDIX C

Derivation of the Transfer Equations for Pristine Ice

Starting with (17) and carrying out the differentiation gives

$$\dot{r}_p^f = \frac{1}{\rho_i} \int_{D_b}^{\infty} \left(n_p(D) \frac{\partial m(D)}{\partial t} + m(D) \frac{\partial n_p(D)}{\partial t} \right) dD$$

$$- m(D_b) n_p(D_b) \frac{\partial D_b}{\partial t}. \tag{C1}$$

The term $\partial D_b / \partial t$ is zero since D_b is constant, and $\partial m(D)/\partial t$ is zero since the frame is Eulerian; thus, (C1) becomes

$$\dot{r}_p^f = \frac{1}{\rho_i} \int_{D_b}^{\infty} m(D) \frac{\partial n_p(D)}{\partial t} dD. \tag{C2}$$

Substitution of (A2) into the above and use of the chain rule allows (C2) to be written in the following form:

$$\dot{r}_p^f = \frac{1}{\rho_i} \int_{D_b}^{\infty} \left\{ \frac{\partial}{\partial D} \left(m(D) \frac{dD}{dt} n_p(D) \right) \right.$$

$$\left. - \frac{\partial m(D)}{\partial D} \frac{dD}{dt} n_p(D) \right\} dD. \tag{C3}$$

Noting that

$$\frac{\partial m(D)}{\partial D} \frac{dD}{dt} = \alpha_m \beta_m D^{\beta - 1} \frac{dD}{dt} = \frac{dm}{dt} \tag{C4}$$

and that the integral

$$\int_{D_b}^{\infty} \frac{\partial}{\partial D} \left(m(D) \frac{dD}{dt} n_p(D) \right) dD$$

$$= m(D_b) \frac{dD}{dt} \bigg|_{D_b} n_p(D_b), \tag{C5}$$

we may write (C3) as

$$\dot{r}_p^f = \frac{1}{\rho_i} m(D_b) \frac{dD}{dt} \bigg|_{D_b} n_p(D_b)$$

$$+ \frac{1}{\rho_i} \int_{D_b}^{\infty} \frac{dm}{dt} n_p(D) dD. \tag{C6}$$

This is (19) in the text given above.

The solution of (19) in the form of (25) given in the text is quite straight forward. Substitution of (11) and (8) into our above equation gives the following form:

$$\dot{r}_p^f = \frac{1}{\rho_i} m(D_b) \left.\frac{dD}{dt}\right|_{D_b} n_p(D_b)$$

$$+ \frac{1}{\rho_i} \Psi \int_{D_b}^{\infty} D n_p(D) dD. \quad (C7)$$

Substitution of the definition of the moments of the incomplete gamma distribution given by (22) into the above, along with the definitions for dD/dt and $m(D)$, gives the final solution of the transfer equation:

$$\dot{r}_p^f = \frac{\Psi}{\rho_i} \alpha_m D_b^2 n(D_b) + \frac{\Psi}{\rho_i} T_p(1, D_b/D_n). \quad (C8)$$

Using similar techniques, equations for the number concentration transfer of pristine ice to snow can be derived; consider the following equation given in the text:

$$\dot{N}_p^f = \frac{d}{dt} \int_{D_b}^{\infty} n_p(D) dD.$$

$$= \int_{D_b}^{\infty} \frac{\partial n_p(D)}{\partial t} - n_p(D_b) \frac{\partial D_b}{\partial t}. \quad (C9)$$

Using the relation given in the text above,

$$\frac{\partial n_p(D)}{\partial t} = -\frac{\partial}{\partial D}\left(\frac{dD}{dt} n_p(D)\right); \quad (C10)$$

then (C9) becomes

$$\dot{N}_p^f = -\int_{D_b}^{\infty} \frac{\partial}{\partial D}\left(\frac{dD}{dt} n_p(D)\right) dD$$

$$= -\left\{\lim_{D\to\infty}\left(\frac{dD}{dt} n_p(D)\right) - \left.\frac{dD}{dt}\right|_{D_b} n_p(D)\right\}.$$

$$(C11)$$

The first term in the equation above goes to zero (as discussed in section 2), so the transfer equation becomes

$$\dot{N}_p^f = \left.\frac{dD}{dt}\right|_{D_b} n_p(D_b). \quad (C12)$$

One can use a similar analysis to derive the equations for the transfers from snow to pristine ice during ice subsaturated conditions. This is not done here [for details of this see Harrington (1994)].

REFERENCES

Abramovitz, M., and I. A. Stegun, 1972: *Handbook of Mathematical Functions.* Dover, 1046 pp.

Arnott, W. P., Y. Y. Dong, and J. Hallett, 1993: Cirrus microphysics observations made during FIRE II: Small particles, high concentrations, and probe comparisons. Preprints, *FIRE Cirrus Science Conf.,* Breckenridge, CO, National Aeronautics and Space Administration, 5–8.

Byers, H. R., 1965: *Elements of Cloud Physics.* The University of Chicago Press, 191 pp.

Cotton, W. R., G. J. Tripoli, R. M. Rauber, E. A. Mulvihill, 1986: Numerical simulation of the effects of varying ice crystal nucleation rates and aggregation processes on orographic snowfall. *J. Climate Appl. Meteor.,* **25,** 1658–1680.

DeMott, P. J., M. P. Meyers, and W. R. Cotton, 1994: Parameterization and impact of ice initiation processes relevant to numerical model simulations of cirrus clouds. *J. Atmos. Sci.,* **51,** 77–90.

Harrington, J. L., 1994: Parameterization of ice crystal conversion processes in cirrus clouds using double-moment basis functions. M. S. thesis, Colorado State University, 135 pp.

Hein, P. F., J. M. Davis, and S. Cox, 1993: Spectral variation of scattering and absorption by cirrus. Preprints, *FIRE Cirrus Science Conf.,* Breckenridge, CO, National Aeronautics and Space Administration, 112–115.

Heymsfield, A., 1975: Cirrus uncinus generating cells and the evolution of cirriform clouds. Part I: Aircraft observations of the growth of the ice phase. *J. Atmos. Sci.,* **32,** 798–808.

Meyers, M. P., 1995: The impact of a two-moment microphysical model on two diverse precipitation events. Ph.D. dissertation, Colorado State University, 120 pp.

——, P. J. DeMott, and W. R. Cotton, 1992: New primary ice nucleation parameterizations in an explicit cloud model. *J. Appl. Meteor.,* **31,** 708–721.

Mitchell, D. L., 1988: Evolution of snow-size spectra in cyclonic storms. Part I: Snow growth by vapor deposition and aggregation. *J. Atmos. Sci.,* **45,** 3431–3451.

——, and W. P. Arnott, 1994: A model predicting the evolution of ice particle size spectra and radiative properties of cirrus clouds. Part II: Dependence of absorption and extinction on ice crystal morphology. *J. Atmos. Sci.,* **51,** 817–832.

——, S. K. Chai, Y. Dong, W. P. Arnott, and J. Hallet, 1993: Importance of aggregation and small ice crystals in cirrus clouds, based on observations and an ice particle growth model. Preprints, *FIRE Cirrus Science Conf.,* Breckenridge, CO, National Aeronautics and Space Administration, 159–162.

Pitter, R. C., 1977: A reexamination of riming on thin ice plates. *J. Atmos. Sci.,* **34,** 684–685.

Pruppacher, H. R., and J. D. Klett, 1978: *Microphysics of Clouds and Precipitation.* D. Reidel, 714 pp.

Schlamp, R. J., and H. R. Pruppacher, 1977: On the hydrodynamic behavior of supercooled water drops interacting with columnar ice crystals. *Pure Appl. Geophys.,* **115,** 805–843.

Srivastava, R. C., and J. L. Coen, 1992: New explicit equations for the accurate calculation of the growth and evaporation of hydrometeors by the diffusion of water vapor. *J. Atmos. Sci.,* **49,** 1643–1651.

Stackhouse, P. W., Jr., and G. L. Stephens, 1990: A theoretical and observational study of the radiative properties of cirrus: Results from FIRE 1986. *J. Atmos. Sci.,* **48,** 2044–2059.

Stephens, G. L., S.-C. Tsay, P. W. Stackhouse Jr., and P. J. Flatau, 1990: The relevance of microphysical and radiative properties of cirrus clouds to climate and climate feedback. *J. Atmos. Sci.,* **47,** 1742–1753.

Tripoli, G. J., and W. R. Cotton, 1981: The use of ice–liquid water potential temperature as a thermodynamic variable in deep atmospheric models. *Mon. Wea. Rev.,* **109,** 1094–1102.

Walko, R. L., W. R. Cotton, J. L. Harrington, and M. P. Meyers, 1995: New RAMS cloud microphysics parameterization. Part I: The single moment scheme. *Atmos. Res.,* **38,** 29–62.